catalysts

MDPI

Review

Iron (Oxyhydr) Oxides in Heterogeneous Fenton Processes: Structure-Activity Relationships in Hydrogen Peroxide Decomposition Pathways

Yi Wang [1,2], Yufan Chen [3] and Deli Wu [1,2,*]

[1] State Key Laboratory of Pollution Control and Resources Reuse, College of Environmental Science & Engineering, Tongji University, Shanghai 200092, China
[2] Shanghai Institute of Pollution Control and Ecological Security, Shanghai 200092, China
[3] Centre for Technology in Water and Wastewater, School of Civil and Environmental Engineering, University of Technology Sydney, Ultimo, NSW 2007, Australia
* Correspondence: wudeli@tongji.edu.cn

Abstract

Iron (oxyhydr)oxides serve as foundational catalysts in heterogeneous Fenton systems, yet their catalytic efficacy varies significantly across distinct mineral species. This review systematically explores the structure-activity relationships governing these variations to provide a clearer understanding of the underlying catalytic mechanisms. The intrinsic physicochemical properties of various mineral phases are examined to elucidate how structural features influence the formation of reactive species, including the highly reactive hydroxyl radical, substrate-dependent high-valent Fe(IV)-oxo species, and selective singlet oxygen generated from hydrogen peroxide (H_2O_2) decomposition. Furthermore, recent optimization strategies aimed at overcoming kinetic barriers and enhancing reaction selectivity are summarized. The discussion concludes with an outlook on future research directions, including catalyst evolution under reaction conditions and the characterization of reactive intermediates, while providing a theoretical framework for the rational design of iron-based catalysts with enhanced stability and oxidative performance.

Keywords: heterogeneous Fenton; iron (oxyhydr)oxides; structure-activity relationship; hydrogen peroxide activation; reactive oxygen species; catalyst design

1. Introduction

The catalytic degradation of refractory organic contaminants remains a formidable challenge in environmental catalysis due to the high stability of complex molecular structures [1,2]. While biological methods often lack the necessary oxidative potential, advanced oxidation processes (AOPs) offer a robust physicochemical solution through the in situ generation of highly reactive oxygen species (ROS) [3–5]. The Fenton reaction, driven by the iron-catalyzed decomposition of hydrogen peroxide (H_2O_2), serves as a benchmark catalytic system for generating hydroxyl radicals ($HO^{\bullet}$) with high redox potential [6,7]. However, the classical homogeneous Fenton process is plagued by inherent operational limitations, primarily the requirement for a narrow acidic pH range (typically around pH 3.0) and the generation of voluminous iron-containing sludge that necessitates costly secondary disposal [8]. These limitations have necessitated a paradigm shift toward heterogeneous Fenton catalysis, which employs solid-state catalysts to enable oxidation over a broader

Check for updates

Academic Editor: Enric Brillas

Received: 11 January 2026
Revised: 26 January 2026
Accepted: 1 February 2026
Published: 4 February 2026

Copyright: © 2026 by the authors. Licensee MDPI, Basel, Switzerland. This article is an open access article distributed under the terms and conditions of the Creative Commons Attribution (CC BY) license.

pH range and enable catalyst recovery, thereby enhancing the practical viability of the technology [9,10].

Within the diverse range of heterogeneous catalysts, naturally occurring and engineered iron (oxyhydr)oxides occupy a prominent position owing to their high abundance in the Earth's crust, environmental biocompatibility, and structural diversity [11,12]. This catalyst family encompasses a wide range of phases, ranging from highly crystalline oxides, such as inverse spinel magnetite (Fe_3O_4) and corundum hematite (α-Fe_2O_3), to oxyhydroxides, including goethite (α-FeOOH) and lepidocrocite (γ-FeOOH), as well as poorly crystalline phases such as ferrihydrite [13]. These minerals not only regulate the natural attenuation of pollutants in geochemical cycles but also serve as the foundational materials for engineered catalytic systems [14]. Their environmental compatibility and ability to activate H_2O_2 at surface active sites make them promising candidates for sustainable water treatment applications. [15].

Despite extensive investigation, the fundamental mechanisms governing the catalytic behavior of different iron (oxyhydr)oxide phases remain under active research and debate. A key unresolved issue is why structurally distinct phases exhibit drastically different reactivities. The interaction between H_2O_2 and mineral surfaces can lead to the formation of diverse oxidizing species, such as $HO^{\bullet}$, high-valent iron–oxo species, or singlet oxygen ($^1O_2$), depending on surface structure, electronic properties, and the surrounding chemical environment. Different reactive species are not universally optimal. For example, in waters rich in natural organic matter (NOM), non-radical oxidants such as $^1O_2$ may be more selective and less susceptible to scavenging than $HO^{\bullet}$. Although many studies report the performance of individual iron minerals, a systematic understanding of how intrinsic physicochemical properties control the type of reactive species formed, and thereby determine suitability under different reaction environments, remains largely lacking in the literature.

To bridge this gap, this review aims to elucidate the structure-activity relationships that shape the heterogeneous Fenton performance of iron (oxyhydr)oxides. Rather than providing a broad survey of all iron-based materials, we limit the scope of this review to heterogeneous Fenton systems driven by iron (oxyhydr)oxides and H_2O_2, and specifically aim to link their phase structure to the formation of reactive species. Following this introduction, Section 2 provides a systematic comparison of the crystallographic and physicochemical properties of major iron (oxyhydr)oxide phases. Section 3 discusses the interfacial activation mechanisms, with a focus on how structural features may influence the formation of reactive species during H_2O_2 decomposition. Section 4 summarizes recent strategies for enhancing catalytic performance, covering approaches such as morphology engineering, defect engineering, and interface design. The review concludes with an outlook on potential future research directions. By integrating perspectives from surface chemistry and solid-state physics, this work seeks to contribute to a theoretical basis for the rational design of efficient iron-based catalysts. By drawing on relevant mechanistic understanding, this review attempts to offer a conceptual framework to support the future design of efficient iron-based catalysts.

2. Physicochemical Properties of Iron (Oxyhydr)oxides

The heterogeneous Fenton reactivity of iron (oxyhydr)oxides is not merely a surface-level effect, but is closely tied to their intrinsic physicochemical properties. While the macroscopic reaction is observed as pollutant degradation, the microscopic efficiency is largely influenced by interaction between H_2O_2 and the solid-state surface [10]. These interactions involve a complex interplay among crystal symmetry, electronic band structures, and surface chemical states [14]. Understanding these properties is therefore a prerequisite

for elucidating the structure-activity relationships that differentiate one mineral phase from another in catalytic systems.

2.1. General Characteristics of Iron (Oxyhydr)oxides

Despite their structural diversity, iron (oxyhydr)oxides are predominantly composed of $Fe(O,OH)_6$ octahedron. The specific connectivity—whether sharing corners, edges, or faces—defines the resulting crystal system and, consequently, the material's stability and reactivity [16]. Generally, these minerals can be classified into oxides, oxyhydroxides, and poorly crystalline hydroxides, each presenting a unique combination of thermodynamic stability and surface active site density [12,17]. The structural framework not only contributes to the mechanical and magnetic properties of the catalyst but also helps define the energetic boundaries for the interfacial electron transfer required for H_2O_2 activation.

2.1.1. Magnetite

Magnetite (Fe_3O_4) is a member of the spinel group and crystallizes in the cubic crystal system with the space group Fd-3m [18]. It is typically crystallographically defined by an inverse spinel structure (AB_2O_4) [19]. In this lattice, trivalent cations occupy the tetrahedral (tet) sites, whereas octahedral (oct) sites are shared by both divalent and trivalent cations [20]. The structural formula is therefore written as $Fe(III)_{tet}[Fe(II)Fe(III)]_{oct}O_4$, forming alternating planes stacked along the [111] direction. Ideally, the Fe(II)/Fe(III) ratio is 0.5, oxidation often leads to nonstoichiometric forms ($Fe_{3-\delta}O_4$) [21]. The presence of structural Fe(II) in the octahedral sites is the defining feature of magnetite, distinguishing it from other iron oxides.

Owing to this inverse spinel configuration, magnetite exhibits unique electronic properties approaching half-metallic character. With a band gap of approximately 0.1 eV [22,23], it facilitates continuous electron exchange between Fe species. Charge transport occurs via rapid electron hopping between Fe-occupied lattice sites [24], as well as the hopping of mobile Fe(II) within the octahedral sublattice [25]. Consequently, magnetite exhibits the highest electrical conductivity among iron oxides (1–10 Sm^{-1}) [19]. This intrinsic high conductivity is critical for heterogeneous catalysis, enabling the charge transfer required for oxidant activation. Additionally, its strong ferrimagnetism allows for energy-efficient separation using external magnetic fields [26], which facilitates easy recovery and reuse, making it a highly practical and sustainable material for various industrial and environmental applications [27].

Catalytic performance is also modulated by particle size and morphology. Nanostructured magnetite (<20 nm in size) exhibits superparamagnetism and surface effects that break structural symmetry, resulting in high surface energy [28]. Wan et al. demonstrated that activity increases significantly as particle size decreases (from 600 to 30nm) owing to the maximized exposure of active sites [29]. At the atomic scale, reactivity is dependent on facet: the (111) facet is frequently associated with higher redox activity due to its abundance of octahedrally coordinated iron atoms compared with the (220) or (400) planes [30,31]. Surface chemistry is governed by amphoteric hydroxyl groups (≡Fe-OH) formed by water dissociation [32], with a point of zero charge (pH_{PZC}) near-neutral (pH~6.5–7.0) [33]. Furthermore, magnetite acts as a functional "nanozyme" with intrinsic peroxidase-like activity, mimicking enzymes such as horseradish peroxidase even under physiological conditions [34].

2.1.2. Maghemite

Maghemite (γ-Fe_2O_3) is a defect-rich, inverse spinel oxide that is isostructural with magnetite. It typically crystallizes in the cubic system (space group $P4_132$ or $P4_332$, depending on vacancy ordering) [35], distinguished by ordered cation vacancies and the absence

of structural Fe(II). Charge neutrality is maintained by vacancies (□) in the octahedral sites, commonly represented as (Fe^{3+}) A[$Fe^{3+}{}_{5/3}\square_{1/3}$]$BO_4$ [19]. This iron-deficient configuration results in a contracted unit cell and dictates the material'–s surface energetics [35]. Importantly, these intrinsic lattice vacancies influence cation migration pathways and possible adsorption geometries for H_2O_2 [36].

Maghemite combines chemical stability with strong ferrimagnetism ($M_s \approx 60$–80 emu g^{-1}) arising from uncompensated spins [37]. Unlike magnetite containing structural Fe(II) which could be oxidized during Fenton reactions, maghemite represents a stable end state, retaining magnetic susceptibility even in oxidative environments. This stability ensures reliable recovery in cyclic operations without phase degradation [38]. Electronically, maghemite is an n-type semiconductor with a band gap of 2.0–2.2 eV, allowing absorption in the visible region [39,40]. However, lacking mixed-valence iron, it behaves as an electrical insulator, suppressing the rapid intervalence charge transfer observed in magnetite [41].

Surface chemistry is characterized by coordination unsaturation compensated by amphoteric hydroxyl groups. The isoelectric point (IEP) is typically around 6.2 [42], indicating that the surface is positively charged in acidic Fenton reaction media. Comparative studies indicate that maghemite has a lower density of proton-active sites (~0.8–1.0 sites nm^{-2}) compared to other phases [43], suggesting either a more acidic surface or the presence of catalytically inert defect sites. These specific surface characteristics influence the initial adsorption of oxidants and the formation of reactive precursor complexes.

2.1.3. Hematite

Hematite (α-Fe_2O_3) constitutes the thermodynamic sink of the iron oxide family, forming as the ultimate transformation product of metastable precursors such as ferrihydrite or goethite [44–46]. It adopts the corundum structure in the trigonal crystal system, where oxygen anions form a rigid hexagonal close-packed (hcp) array, and Fe(III) cations occupy two-thirds of the octahedral interstices [19,47]. This dense atomic packing confers exceptional structural rigidity and an extremely low solubility product ($K_{sp} \approx 10^{-44}$), rendering it highly resistant to dissolution [44,45]. While this stability ensures catalyst longevity, it however kinetically disfavors the surface restructuring or iron leaching required during certain Fenton cycles.

The surface of hematite undergoes rapid oxidation in water [48–50]. The nature of this hydration is anisotropic: for example, water dissociates differently on the Fe-terminated (0001) surface compared with the (104) surface [48,50]. In general, hematite exhibits a lower surface hydroxyl density than ferrihydrite, limiting its adsorption capacity [51]. Its PZC ranges between 7.0 and 9.0 [52], governing the electrostatic interaction with anionic species under neutral pH conditions. Through morphology control, hematite can be synthesized to expose specific facets (e.g., nanoplates or nanorods), for which variations in atomic coordination tune the surface energy and reactivity [53,54].

Electronically, hematite is an n-type semiconductor with an indirect band gap of 2.1–2.2 eV [55], allowing absorption in the visible region. However, its charge transport is limited by a small polaron hopping mechanism, resulting in low carrier mobility and short diffusion lengths (2–4 nm) [17,56]. Consequently, effective catalytic turnover requires surface redox reactions to proceed faster than bulk recombination. Unlike magnetite, hematite is weakly ferromagnetic or antiferromagnetic, making magnetic separation challenging [31].

2.1.4. Goethite

Goethite (α-FeOOH) is the most thermodynamically stable iron (oxyhydr)oxide under ambient conditions [57,58]. It crystallizes in the orthorhombic system with a structural motif composed of distorted $FeO_3(OH)_3$ octahedra edge-sharing to form double chains

along the [001] direction. These chains are linked through corner-sharing oxygens to create a rigid 2 × 1 tunnel structure occupied by hydrogen atoms [19]. This network of Fe–O bonds and bonding within the bulk confers exceptional stability against dissolution and phase transformation.

The structural anisotropy gives rise to its characteristic acicular (needle-like) growth, resulting in a dominance of prismatic (110) faces in the specific surface area and terminal (021) or (001) faces [59]. Reactivity is intrinsically linked with surface hydroxyl configurations: the (110) face exposes alternating rows of singly, doubly, and triply coordinated hydroxyls, while the terminal (021) face is enriched in singly coordinated groups with higher proton affinity and greater lability [60]. CD-MUSIC modeling confirms that protonation constants are facet-dependent, thereby creating a heterogeneous surface charge distribution [61]. Molecular dynamics simulations further reveal that interfacial water structure varies significantly between these faces [62].

Goethite behaves as an n-type semiconductor with a band gap of 2.1–2.5 eV [63]. While pure synthetic goethite has exhibits a wider gap, cation substitution (e.g., Al) in natural specimens can significantly modulate the electronic structure, narrowing the gap to ~2.25 eV [64]. These electronic band positions largely determine the thermodynamic feasibility of interfacial electron transfer, thereby setting the energetic boundaries for redox cycling [65].

2.1.5. Lepidocrocite

Lepidocrocite (γ-FeOOH) is structurally distinct from goethite, characterized by a layered orthorhombic structure [19,66]. Its $FeO_3(OH)_3$ octahedra form zigzag sheets stacked along the b-axis, held together primarily by hydrogen bonds [19,67]. This weak interlayer interaction imparts pronounced anisotropy, typically resulting in lath-like or platelet morphologies. As a consequence of this open architecture, synthetic lepidocrocite often exhibits a relatively high specific surface area (15–150 $m^2\ g^{-1}$) [68]. Thermodynamically, lepidocrocite is metastable relative to goethite and hematite [69]. Upon thermal treatment, it undergoes topotactic transformation to maghemite; in aqueous suspensions with Fe(II), it readily transforms to goethite via dissolution-reprecipitation [70,71]. This metastability is highly relevant to Fenton catalysis, suggesting that the phase may evolve dynamically during operation. Its surface chemistry is governed by hydroxyl groups with a PZC in the circumneutral range (pH~6.7–7.5) [72,73], facilitating electrostatic interactions under acidic conditions. Electronically, lepidocrocite behaves as an n-type semiconductor with a band gap of 2.06–2.37 eV [40]. This enables visible light absorption, supporting photo-assisted Fenton processes where photogenerated carriers drive redox cycling [74].

2.1.6. Ferrihydrite

Ferrihydrite is a ubiquitous, poorly crystalline mineral representing the initial precipitate of rapid Fe(III) hydrolysis. Characterized by nanoscale dimensions (<5 nm) and an extensive specific surface area, it exhibits properties that are fundamentally different from those of crystalline phases. Its structure remains debated; historically described as a multiphase mixture, the single-phase model proposed by Michel et al. proposes a structure containing ~20% tetrahedral Fe(III) and 80% octahedral Fe(III) [75]. The presence of tetrahedral iron may be relevant for catalysis, as it is associated with locally distorted bond lengths and distinct electronic states [76]. More recent views describe it as a dynamic nanocomposite of coherent motifs separated by disordered boundaries [77,78].

Ferrihydrite possesses the highest surface area among iron oxides, with BET values of 200–400 $m^2\ g^{-1}$, reactive surface area in suspension may exceed 600 $m^2\ g^{-1}$ [79]. The surface is dominated by singly coordinated (≡Fe-OH) groups active in ligand-exchange

reactions [80]. Its hydration structure can also function as a hole-storage layer in photo-driven processes [81]. Ferrihydrite is metastable and prone to transform into goethite or hematite [57]. This transformation is highly sensitive to environmental conditions; notably, adsorbed Fe(II) accelerates recrystallization by facilitating electron transfer through the lattice [82]. Conversely, impurities such as organic matter can stabilize the nanoparticulate structure [83]. This dynamic nature contributes to making ferrihydrite a highly reactive yet relatively unstable component in Fenton systems.

2.2. Comparison of Physicochemical Properties

To clarify the distinct roles of specific iron (oxyhydr)oxides in heterogeneous Fenton(-like) systems, it is valuable to move beyond individual mineral descriptions and to develop a comparative framework. The variations in catalytic efficiency and stability among these phases are not arbitrary random but arise from quantifiable differences in their crystal packing, electronic transport capabilities, surface chemical states, and intrinsic reactivity. This section provides a comparative analysis across the six minerals discussed, highlighting the physicochemical descriptors that influence their performance.

2.2.1. Crystal Packing and Pore Geometry

The structural openness of the mineral lattice plays a key role in determining the accessibility of active sites and the diffusion limitations for reactants. A clear hierarchy exists in terms of porosity and atomic density among the iron oxides. Hematite and magnetite tend to exhibit the most dense and rigid crystal structures within this mineral group [19]. These minerals consist of compact oxygen frameworks based on close-packed arrays with minimal internal porosity. Consequently, catalytic reactions on these phases primarily occur on the external geometric surface, as the diffusion of reactants into the dense crystal bulk is spatially restricted [31]. While this high atomic density confers superior thermodynamic stability, it may also constrain the number of accessible active sites per unit mass relative to more open or disordered structures [79].

An intermediate degree of structural openness is observed in goethite and lepidocrocite. Goethite is characterized by a 2×1 tunnel structure, while lepidocrocite exhibits a layered architecture held together by hydrogen bonds [19,67]. As demonstrated by Hu et al., these anisotropic structures can accommodate a higher density of lattice vacancies compared to the dense oxides [84]. Specifically, the interlayer spaces in lepidocrocite provide a unique chemical environment distinct from the dense packing of hematite, thereby potentially allowing enhanced interaction with smaller ionic species.

Distinct from the dense, well-crystallized phases (e.g., hematite, magnetite), ferrihydrite exists as a disordered assembly of nanoparticles rather than a monolithic crystal. This unique aggregation gives rise to extensive intra-aggregate microporosity [79]. Dai and Wang highlighted that this specific pore geometry is often overlooked yet critical; the abundant micropores in ferrihydrite create steric confinement effects distinct from the external surface adsorption dominant in crystalline phases [85]. This structural distinction implies that adsorption and catalytic reactions on ferrihydrite are governed by pore-filling mechanisms, thereby offering a reactive surface area (>600 $m^2\ g^{-1}$) significantly exceeding that of its crystalline counterparts (typically < 150 $m^2\ g^{-1}$) [68,79]. The structural characteristics and H_2O_2 decomposition performance of these minerals are summarized in Table 1.

Table 1. Structural characteristics and H_2O_2 decomposition performance of representative bulk-phase iron (oxyhydr)oxides.

Mineral	Formula	Crystal System [a]	Space Group [a]	Polyhedral Unit [b]	Pore Character [c]	Density [d] (g cm^{-3})	BET [d] (m^2 g^{-1})	$k_{obs,\ H_2O_2}$ (min^{-1}) [d]
Magnetite	Fe_3O_4	Cubic	$Fd\bar{3}m$	FeO_6 FeO_4	Non-porous	5.18	42.5	0.303
Maghemite	γ-Fe_2O_3	Cubic	$P4_132$	FeO_6 FeO_4	Non-porous	4.87	29.8	0.105
Hematite	α-Fe_2O_3	Hexagonal	$R\bar{3}c$	FeO_6	Non-porous	5.26	7.36	0.011
Goethite	α-FeOOH	Orthorhombic	Pbnm	FeO_6	Non-porous; Mesoporous	4.26	33.4	0.050
Lepidocrocite	γ-FeOOH	Orthorhombic	Cmcm	FeO_6	Mesoporous	4.09	67.3 [e]	-- [f]
Ferrihydrite	$Fe_5HO_8{\cdot}4H_2O$	Hexagonal	$P6_3mc$	FeO_6 FeO_4	Microporous	3.96	252.7	1.985

[a] Crystallographic data are referenced from Lai et al. [86]. [b] FeO_6 and FeO_4 denote octahedral and tetrahedral coordination, respectively, describing the geometry illustrated in Figure 1. [c] General qualitative descriptions of porosity refer to minerals synthesized via conventional methods, excluding engineered nanostructures. [d] Values for Density, BET surface area, and pseudo-first-order rate constants (k_{obs}) for H_2O_2 decomposition are cited from the comparative study by Molamahmood et al. [87]. Experimental conditions: [H_2O_2] = 7.2 mM, [iron mineral] = 2 g/L, pH = 5.0. [e] BET surface area for lepidocrocite is cited from Huang et al. (2023) [88] as it was not included in the main comparative study [87]. [f] Lepidocrocite was not included in the kinetic dataset of [88].

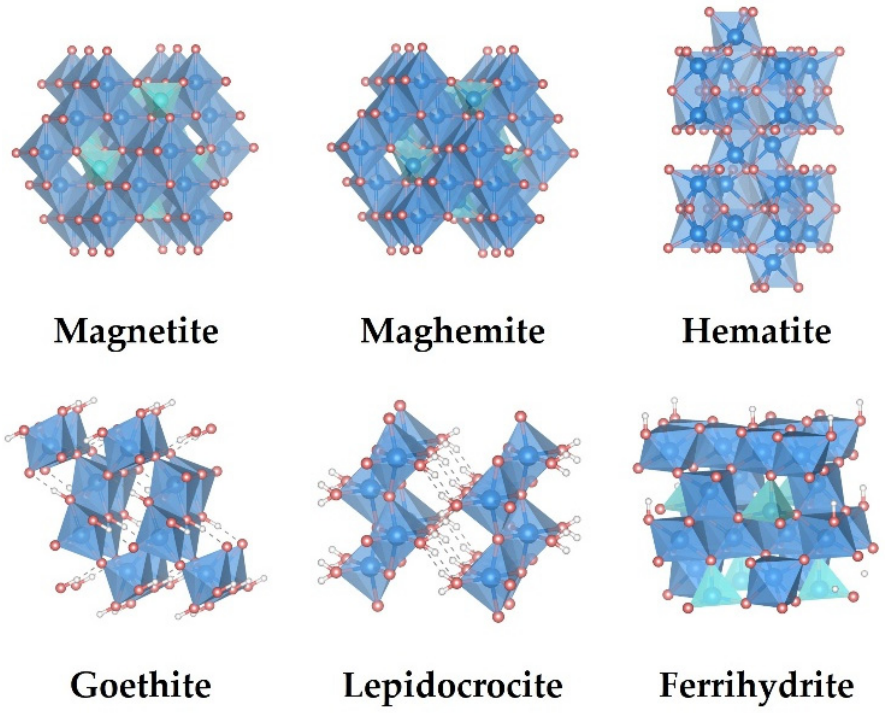


Figure 1. Polyhedral representations of the crystal structures of major iron (oxyhydr)oxides discussed in this review.

2.2.2. Conductivity and Electronic Structure

The ability of the catalyst to mediate electron transfer between iron centers and H_2O_2 is an important factor influencing reaction kinetics. From an electronic transport perspective, the minerals can generally be classified into conductors, semiconductors, and near-insulators. Magnetite stands out as the sole conductor among the group, with electrical conductivity (10^2–10^3 Ω^{-1} cm^{-1}) orders of magnitude higher than other iron oxides [19]. It represents the primary phase that facilitates rapid bulk electron transport, enabling the bulk of the material to participate in charge redistribution during catalysis via the intervalence charge transfer mechanism [24]. In contrast, hematite, goethite, lepidocrocite, and ferrihydrite typically behave as n-type semiconductors with markedly lower conductivity (<10^{-2} Ω^{-1} cm^{-1}) [56,63]. Li et al. noted that while their band gaps are similar (ranging between 2.0 and 2.5 eV), their charge transfer mechanisms differ from magnetite. Rather

than bulk conduction, these minerals rely on surface-localized redox cycles. Xu and Liu recently clarified that for these semiconductor minerals, the electron transfer is often mediated through the capacitive charging and discharging of surface Fe(III)/Fe(II) couples rather than intrinsic metallic conduction [89].

Maghemite represents the least conductive phase. Although it is isostructural with magnetite, the absence of Fe(II) and the presence of ordered vacancies render it effectively insulating [41]. Consequently, electron transfer on maghemite is kinetically restricted and largely dependent on localized surface defects rather than bulk transport pathways [36].

2.2.3. Surface Hydroxyl Density and Acidity

The density and nature of surface hydroxyl groups (-OH) strongly influence the adsorption capacity for H_2O_2 and organic substrates. Ferrihydrite exhibits the highest surface hydroxyl density, attributable to its high defect density and microporosity [80]. This is followed by lepidocrocite. Beyond total density, studies on lepidocrocite have indicated that the specific configuration of hydroxyl groups may also be significant. For instance, Qin et al. reported facet-dependent behavior in lepidocrocite, observing that singly coordinated hydroxyls (μ_1-OH) on (010) facets were primarily associated with substrate adsorption, whereas triply coordinated hydroxyls (μ_3-OH) on (001) facets appeared more efficient for radical generation [90].

Regarding surface acidity, the pH_{PZC} is another parameter summarizing the surface electrochemical state. Most crystalline iron oxides possess pH_{PZC} values in the circumneutral range. Consequently, under acidic Fenton conditions, these surfaces are expected to carry a net positive charge. Recent literature has discussed how this surface charge might influence catalytic behavior beyond physical adsorption. This effect is often linked to the modulation of the protonation state of surface active sites. Theoretical calculations on iron coordination environments by Liu et al. indicated that a proton-rich environment could increase the energy barrier for H_2O_2 deprotonation, a step often regarded as necessary for precursor complex formation [91]. These findings suggest that the proximity of the operating pH to the pH_{PZC} may influence the proportion of kinetically active sites on the catalyst surface. The typical pH_{PZC} ranges for these minerals are listed in Table 2.

Table 2. Typical ranges of point of zero charge for representative iron (oxyhydr)oxides.

Mineral	Formula	pH_{PZC} [a]
Magnetite	Fe_3O_4	6.5–6.9
Maghemite	γ-Fe_2O_3	6.5–7.3
Hematite	α-Fe_2O_3	7.2–9.1
Goethite	α-FeOOH	8.1–8.6
Lepidocrocite	γ-FeOOH	7.1–7.8
Ferrihydrite	$Fe_5HO_8 \cdot 4H_2O$	7.6–8.0

[a] Data are referenced from Kosmulski (2009) [42]. The pH_{PZC} values vary depending on the synthesis method and hydration state.

3. H_2O_2 Decomposition Mechanisms on Iron (Oxyhydr)Oxide Surfaces

The catalytic efficiency of heterogeneous Fenton systems is strongly influenced by the interaction mechanism between H_2O_2 and the catalyst surface. Unlike the homogeneous Fenton reaction, where interactions are governed largely by fluid-phase mixing and stochastic ion collision, the heterogeneous process employing iron (oxyhydr)oxides is instead governed by complex interfacial dynamics. The efficiency of the system does not depend solely on oxidant generation but is dictated by a sequence of coupled steps: the mass transport of reactants, surface complexation, the specific electronic activation of H_2O_2, which determines the nature of the oxidizing species, and the spatial confinement of the oxidation event.

3.1. Fundamental Steps of Interfacial Reactions

The introduction of a solid phase significantly increases the mechanistic complexity of the system. The decomposition of H_2O_2 on iron (oxyhydr)oxide surfaces is widely described by the surface complexation model, which draws an analogy with homogeneous coordination chemistry yet occurs exclusively at the solid–liquid interface [92,93]. However, before chemical activation can occur, reactants must overcome mass-transfer resistance to reach the active sites. The overall process involves a multistep sequence: reactant transport to the interface, competitive adsorption, surface chemical reaction, and the subsequent desorption or reaction of products.

The process is typically initiated by the adsorption of H_2O_2 onto the catalyst surface. H_2O_2 undergoes ligand exchange with surface hydroxyl groups or coordinated water molecules, coordinating with surface iron ≡Fe(III) sites. This process results in the formation of an inner-sphere precursor complex, commonly represented as $\equiv Fe(III)(O_2H)^-$ [92,93].

$$\equiv Fe(III) + H_2O_2 \rightleftharpoons \equiv Fe(III)(O_2\,H)^- + H^+ \quad (1)$$

Following surface complexation, the reaction pathway diverges markedly depending on the mineralogy and iron oxidation state of the iron (oxyhydr)oxide. For Fe(III)-dominated minerals such as goethite, hematite, and ferrihydrite, the reaction proceeds via an intramolecular ligand-to-metal electron transfer. During this process, the peroxo ligand donates an electron to the iron center, reducing surface Fe(III) to Fe(II) and generating either a hydroperoxyl radical ($HO_2^\bullet$) or a superoxide anion ($O_2^{\bullet-}$) [92,94].

$$\equiv Fe(III)(O_2H)^- \rightarrow \equiv Fe(II) + HO_2^\bullet / O_2^{\bullet-} \quad (2)$$

Within the Haber-Weiss cycle, the reduction in surface Fe(III) to Fe(II) is generally regarded as he rate-limiting step due to a high thermodynamic barrier, resulting in the commonly observed induction period in Fenton-like reactions catalyzed by Fe(III) oxides [94]. In contrast, for minerals containing intrinsic structural Fe(II) such as magnetite and siderite, the reaction bypasses this slow reduction step. The surface structural Fe(II) can react directly with H_2O_2 via a heterogeneous Fenton-like step, thereby exhibiting superior initial activity [95,96]. This mechanistic distinction underscores why controlling the Fe(II)/Fe(III) ratio and its spatial distribution is a key strategy in catalyst design.

$$\equiv Fe(II) + H_2O_2 \rightarrow \equiv Fe(III) + HO^\bullet + OH^- \quad (3)$$

While H_2O_2 adsorption is a prerequisite, the adsorption behavior of the target organic pollutant plays a dual role in the reaction mechanism. Recent mechanistic studies have clarified this trade-off. On one hand, pollutant adsorption can enhance degradation by minimizing diffusion distances to reactive oxidants. On the other hand, strong adsorption can lead to active site saturation. Chen et al. demonstrated this using ferrihydrite: while formate enables rapid catalytic turnover due to weak adsorption, oxalate saturated the available surface active sites [97]. This competitive adsorption inhibited the access of H_2O_2 and suppressed the regeneration of active ≡Fe(II) sites, thereby stalling the overall reaction despite a high thermodynamic affinity. Thus, the overall efficiency is constrained by the competition between the oxidant and the substrate for limited surface sites.

3.2. Reactive Species Formed from H_2O_2 Decomposition

Once an active surface complex is formed, the dissociation of the Fe-H_2O_2 intermediate largely determines the efficacy of the Fenton system. The decomposition does not follow a

single reaction trajectory; rather, variations in crystal structure, surface electronic states, and the nature of the co-adsorbed substrate steer the reaction toward different reactive species formed. Crucially, the identification of these specific oxidants—whether freely diffusing $HO^{\bullet}$, surface-confined high-valent iron (Fe(IV)), or $^1O_2$—is not absolute. It is strictly contingent upon reaction parameters (e.g., pH, electrolytes) and the limitations of detection methodologies, such as probe selectivity and potential interference from iron leaching.

3.2.1. Hydroxyl Radical and Spatial Confinement

In the classical heterogeneous Fenton mechanism, the interaction between surface ≡Fe(II) and H_2O_2 induces homolytic cleavage of the O-O bond. This process yields the hydroxyl radical ($HO^{\bullet}$), a powerful and non-selective oxidant capable of degrading most refractory organic pollutants [93].

$$\equiv Fe(II) + H_2O_2 \rightarrow \equiv Fe(III) + HO^{\bullet} + OH^{-} \quad (4)$$

Historically, it was debated whether these radicals remain bound to the surface or are released into the bulk solution. Recent advancements using reactive-transport modeling and in situ characterization have refined this understanding toward the diffused radical model. Chen et al. and Zhang et al. provided evidence that while $HO^{\bullet}$ is generated at the surface, it subsequently desorbs and diffuses into a spatially confined interfacial boundary layer, typically extending approximately 200 nm from the particle surface [97,98]. Within this boundary layer, $HO^{\bullet}$ concentrations are orders of magnitude higher than those in the bulk solution.

However, this confinement effect depends on specific reaction conditions. For instance, Zhang et al. reported that high ionic strength could compress the electric double layer (Debye length), which was observed to diminish the degradation kinetics of confined pollutants. Furthermore, they suggested that the enrichment of pollutants might depend on the electrostatic matching (Zeta potential) between the catalyst surface and the target molecules [98]. Additionally, Chen et al. proposed that neutral scavengers (e.g., alcohols) may have limited accessibility to this charged boundary layer compared to electrostatically attracted substrates [97]. These practical limits should be carefully considered when evaluating reaction mechanisms in diverse matrices.

3.2.2. High-Valent Fe(IV)-Oxo Species

High-Valent Fe(IV)-oxo species were proposed in the homogeneous Fenton system. Researchers have proposed that, in addition to the classical homolytic pathway generating $HO^{\bullet}$, Fe(II) and H_2O_2 may undergo two-electron transfer via heterolytic cleavage of the O–O bond, producing high-valent iron species [99]. Pestovsky et al. (2005) successfully characterized the aqueous $[(H_2O)_5Fe^{IV} = O]^{2+}$ species using Mössbauer spectroscopy and X-ray absorption spectroscopy, confirming its existence as an independent reactive intermediate [100]. Bataineh et al. (2012) [101] further found that in non-coordinating buffered media at pH 6–7, the probe molecule dimethyl sulfoxide (DMSO) was selectively oxidized to dimethyl sulfone ($DMSO_2$). This phenomenon was attributed to a specific oxygen atom transfer reaction by Fe(IV), providing direct evidence for the generation of Fe(IV) in homogeneous systems [101].

In heterogeneous Fenton systems, although some studies have reported characteristic signals of Fe(IV), these findings are accompanied by certain questions. Chen et al. (2022) observed in a ferrihydrite-catalyzed Fenton system that the characteristic Fe(IV) product $PMSO_2$ was only detectable when using a high concentration (20 mM) of the probe molecule PMSO, while it could not be detected at lower probe concentrations [102]. The researchers proposed two explanations for this: (i) the generated Fe(IV) might be largely confined

to the catalyst surface or near-surface regions, requiring high substrate concentrations to drive its mass transfer and reaction; (ii) Fe(IV) might be rapidly consumed by H_2O_2 or water, preventing effective contact with low-concentration probes [102]. These observations raise a critical question regarding whether the absence of Fe(IV) signals implies it was not generated, or if the species is simply consumed in situ too rapidly to be captured by bulk-phase probes.

Furthermore, studies have pointed out that the probe molecules used to identify Fe(IV) may themselves perturb the reaction system, leading to misleading signals. Chen et al. (2023) indicated that the widely used probe methyl phenyl sulfoxide (PMSO), after reacting with coexisting $HO^{\bullet}$ in the system, could form complexes with Fe(III) through its oxidative degradation products, significantly altering the reduction potential and reaction kinetics of the iron species, thereby artificially promoting $PMSO_2$ formation [103]. This implies that $PMSO_2$ observed in heterogeneous systems may not originate directly from initially generated Fe(IV) intermediates, but could instead be produced via other pathways (such as the formation of highly reactive iron-peroxo or iron-ligand complexes) induced by the degradation products of PMSO itself. Therefore, results from using probe molecules to detect Fe(IV) are highly dependent on the specific reaction system and may be significantly influenced by side reactions triggered by the probe.

3.2.3. Selective Singlet Oxygen

Unlike $HO^{\bullet}$ and high-valent iron-oxo species discussed in previous sections, $^1O_2$ is a non-radical reactive ROS characterized by its high selectivity toward electron-rich organic contaminants. Although the molybdate ion-catalyzed H_2O_2 disproportionation reaction is found to produce $^1O_2$ efficiently [104], $^1O_2$ has been considered to be unimportant in Fenton chemistry for several decades.

However, Yang et al. (2019) [105] claimed to find evidence that $^1O_2$ is the primary oxidant in a Fenton-like system, which is catalyzed by confining Fe_2O_3 nanoparticles inside multiwalled carbon nanotubes with inner diameter of ~7 nm. Their evidence included [105]: (i) observed ESR spectra assigned to an $^1O_2$ adduct, namely 2,2,6,6-tetramethyl-4- piperidinol-N-oxyl radical, when using 2,2,6,6-tetramethyl-4-piperidinol as the trapping agent [106,107] but non-observable ESR signal of an $HO^{\bullet}$ adduct when using DMPO as the trapping agent; (ii) the formation of anthracene endoperoxide, which is used as the indicative product of $^1O_2$, from the oxidation of anthracene derivative [108,109]; and (iii) almost 100% conversion of furfuryl alcohol (FFA) to three indicative oxidation products generated from $^1O_2$ [110,111]. Yang et al. attributed this phenomenon to a nanoconfinement effect, suggesting that $^1O_2$ generation is kinetically and thermodynamically challenged in the bulk phase [106]. In addition, Scaria and Nidheesh (2022) [112] observed that in an acidic Fe_3O_4-rGO/H_2O_2 system (pH 3), the degradation was inhibited more significantly by sodium azide (NaN_3, a $^1O_2$ scavenger) than by tert-butanol (a $HO^{\bullet}$ scavenger). Based on this, they proposed that the contribution of $^1O_2$ and superoxide radicals ($O_2^{\bullet-}$) might exceed that of $HO^{\bullet}$ in this specific system [112]. However, such a conclusion based on chemical-quenching experiments is debatable and needs to be corroborated by more direct analytical techniques.

In summary, the specific ROS generated in heterogeneous Fenton systems is governed by a complex interplay between the intrinsic properties of the iron mineral and the extrinsic reaction conditions. While $HO^{\bullet}$ are ubiquitous, alternative oxidants like Fe(IV) and $^1O_2$ can dominate under specific constraints such as nanoconfinement or neutral pH. From an application perspective, the choice between these pathways depends on the specific target pollutants. The radical pathway, driven by non-selective $HO^{\bullet}$, is generally preferable for the complete mineralization of recalcitrant organic pollutants due to its high redox

potential [6]. In contrast, non-radical pathways mediated by $^1O_2$ or Fe(IV) offer distinct advantages for the selective removal of electron-rich contaminants, particularly in complex water matrices where the scavenging of HO• significantly inhibits efficiency [113]. Table 3 provides a comparative overview of H_2O_2 activation pathways and dominant reactive species for representative iron (oxyhydr)oxides.

Table 3. Summary of H_2O_2 activation pathways and dominant reactive species for representative iron minerals.

Mineral	Key Characteristics [a]	Activation Pathway [b]	Dominant Product [c]	Reaction Conditions (pH/H_2O_2/Cat.)	Pollutant [d]	Reference
Magnetite	Structural Fe(II); Nanoparticles	Homogeneous Fenton (due to leaching); Heterogeneous Radical Pathway	HO•	pH 3.0 12 mM 1.0 g/L	2,4-DCP	[114]
Magnetite	Nanoconfinement (Supported on AAO)	Heterogeneous Radical Pathway	HO•	pH 3.25 1 mM --	pCBA	[98]
Magnetite	Structural Fe(II)	Heterogeneous Radical Pathway; Non-productive Disproportionation	HO•, $O_2^{\bullet-}$, O_2	pH 3–9 7.2 mM 2.0 g/L	BA	[87]
Hematite	--	Heterogeneous Radical Pathway	HO•	pH 3–9 7.2 mM 2.0 g/L	BA	[87]
Hematite	Surface oxygen vacancies	Non-productive Disproportionation; Heterogeneous Radical Pathway	O_2; HO•(Minor)	pH 4.5 10 mM 1.0 g/L	DEP	[115]
Hematite	Nanoconfinement (Inside CNTs)	Non-Radical Pathway	$^1O_2$	pH 3–9 50 mM 0.015 g/L	MB	[105]
Hematite	Surface area	Heterogeneous Radical Pathway	HO•	pH 4.0 0.1 mM–1 M --	Formate	[92]
Goethite	Exposed facets (Needle-like)	Heterogeneous Radical Pathway	HO•, $O_2^{\bullet-}$	pH 6–8 14.7 mM 0.5 g/L	BSA	[88]
Goethite	Surface Area	Heterogeneous Radical Pathway (Surface complexation)	HO•	pH 7.0 1–10 mM 0.2–3 g/L	BuCl	[93]
Goethite	Surface oxygen vacancies	Heterogeneous Radical Pathway	HO•	pH 4.5 10 mM 1.0 g/L	DEP	[115]
Goethite	Surface Area	Heterogeneous Radical Pathway	HO•	pH 4.0 0.1 mM–1 M --	Formate	[92]
Lepidocrocite	Exposed facets (Flake-like)	Heterogeneous Radical Pathway	HO•	pH 6–8 14.7 mM 0.5 g/L	BSA	[88]
Feroxyhyte	--	Non-productive Disproportionation; Heterogeneous Radical Pathway	O_2; HO• (Minor)	pH 3–9 7.2 mM 2.0 g/L	BA	[87]
Ferrihydrite	Surface ≡Fe(III) complexation sites	Non-Radical Pathway(for complexing pollutants); Heterogeneous Radical Pathway (for non-complexing)	ET (for BA, PAA, 4-HBA); HO• (for Others)	pH 3–5 ~10 mM 0.5 g/L	BA, PAA, 4-HBA; ATZ, NB, PMSO	[116]
Ferrihydrite	--	Heterogeneous Radical Pathway; Non-Radical Pathway	HO•; Fe(IV) (Possible) [e]	pH 3–6 10 mM --	Formate, PMSO	[102]
Ferrihydrite	Interfacial adsorption layer	Heterogeneous Radical Pathway	HO•	pH 4.0 0.1–10 mM 0.2 g/L	Formate	[97]
Ferrihydrite	Catalase-like active centers (≡Fe-OH)	Catalase-like Process	O_2	pH 4–9 100 mM 0.2 g/L	--	[117]
Ferrihydrite	--	Non-productive Disproportionation; Heterogeneous Radical Pathway	O_2; HO• (Minor)	pH 3–9 7.2 mM 2.0 g/L	BA	[87]
Ferrihydrite	Surface oxygen vacancies	Non-productive Disproportionation; Heterogeneous Radical Pathway	O_2; HO• (Minor)	pH 4.5 10 mM 1.0 g/L	DEP	[115]
Ferrihydrite	--	Heterogeneous Radical Pathway	HO•	pH 4.0 1 mM 0.2 mM Fe	Formate	[92]

[a] Blank cells (--) indicate that the structural key characteristic was not stated in the cited literature. [b] Activation pathway is referenced from Ref. [15]; Catalase-like Process is referenced from Ref. [117]. [c] Oxygen is listed only for studies that explicitly detected or focused on its production. The absence of oxygen in other entries does not preclude its formation but indicates it was not monitored or reported in those studies. [d] Refer to the List of Abbreviations for full names of target pollutants. [e] Fe(IV) species is a possible intermediate proposed by Chen (Y.) et al. (2022) [102] but requires further verification.

3.3. Regulation Mechanism of Phase Structure on Reaction Pathways

The phase structure of iron (oxyhydr)oxides significantly influences the decomposition pathway of H_2O_2 by modulating the intrinsic physicochemical properties of the catalyst surface. This influence is exerted mainly through three interconnected factors: the geometric configuration of surface active sites, the electronic structure governing charge transport, and the interfacical microenvironment. Together, these factors jointly control the reaction energy barrier and pathway selectivity, thereby establishing the physical basis for the variations in catalytic efficiency observed among different mineral phases.

3.3.1. Geometric Configuration and Atomic Coordination

The primary mechanism by which phase structure regulates Fenton activity lies in the spatial arrangement of surface atoms. This microscopic arrangement manifests either as the ordered termination of specific facets in crystalline minerals or as the disordered distortion of local coordination environments in low-crystallinity materials. Accordingly, the structure-activity relationship dictates that specific geometric configurations govern both the coordination unsaturation and the structural flexibility of active sites, thereby controlling the adsorption mode of H_2O_2 as well as the activation energy required for O-O bond cleavage.

In well-crystallized iron (oxyhydr)oxides, the crystallographic orientation of exposed facets directly dictates the geometrc spacing and electronic state of surface atoms, acting as a critical variable in regulating reaction kinetics. As a consequence, crystallographic anisotropy results in significant differences in the density of coordination-unsaturated iron atoms (Fe_{CUS}). Wang et al. demonstrated in their study of hematite (α-Fe_2O_3) that high-surface-energy facets (e.g., (101)) typically expose a greater number of coordination-deficient iron sites compared to low-surface-energy facets (e.g., (001)). This elevated density of Fe_{CUS} increases the likelihood of productive collisions between H_2O_2 molecules and the catalyst surface [118].

However, the geometric configuration of active sites is often more than mere site density. Huang et al. (2016) [119] elucidated the influence of atomic spacing on activation energy within a density functional theory (DFT)-based energetic span framework. Their research indicated that the hematite (110) facet possesses specific binuclear iron spacing capable of inducing H_2O_2 to form a bidentate coordination configuration. This geometric matching exerts physical tension on the O-O bond, causing significant bond elongation and effectively lowering the activation energy for homolytic cleavage into $HO^{\bullet}$. In contrast, the (001) facet tends to favor monodentate coordination, leading to less efficient activation [119]. Furthermore, steric hindrance arising from the topological structure and local coordination environment of surface atoms also determines the reaction pathway. Huang et al. (2019) [120] elucidated this by comparing different morphologies of hematite nanoparticles, finding that the (001) facet exhibited Fenton activity superior to that of the (012) facet. The atomic configurations of these facets are illustrated in Figure 2. Theoretical modeling revealed that the (001) facet is dominated by 3-fold undercoordinated iron sites (Fe_{3uc}), which are more intrinsically reactive and easier to reduce compared to the 1-fold undercoordinated sites (Fe_{1uc}) found on the (012) facet. Kinetic analysis within an energetic span framework confirmed that this coordination advantage significantly lowers the apparent activation energy (E_a) for the (001) facet (17.13 kcal/mol) compared to the (012) facet (24.94 kcal/mol), thereby facilitating more efficient $HO^{\bullet}$ generation [120]. In contrast to highly ordered crystal structures, lowering crystallinity or introducing amorphous phases offers an alternative strategy for enhancing activity based on structural disorder. Numerous studies indicate that low-crystallinity iron minerals (e.g., amorphous FeOOH, ferrihydrite) often exhibit Fenton reactivity superior to that of well-crystallized minerals

such as hematite, magnetite [121]. This enhancement is primarily attributed to the lack of long-range order in amorphous structures, which are characterized by a high abundance of distorted coordination polyhedra. Moreover, a decrease in crystallinity is typically accompanied by the formation of a high density of lattice defects. Wang et al. observed that, among ferrihydrites with varying degrees of crystallinity, lower-crystallinity samples produced higher yields of reactive oxygen species under irradiation. Mechanistic analysis revealed that although crystallinity had a limited effect on photon-to-electron conversion efficiency, the abundant defect sites significantly facilitated the reduction in O_2 by conduction band electrons (the rate-limiting step for $O_2^{\bullet-}$ generation), thereby accelerating the in situ generation and subsequent activation of H_2O_2 [122].

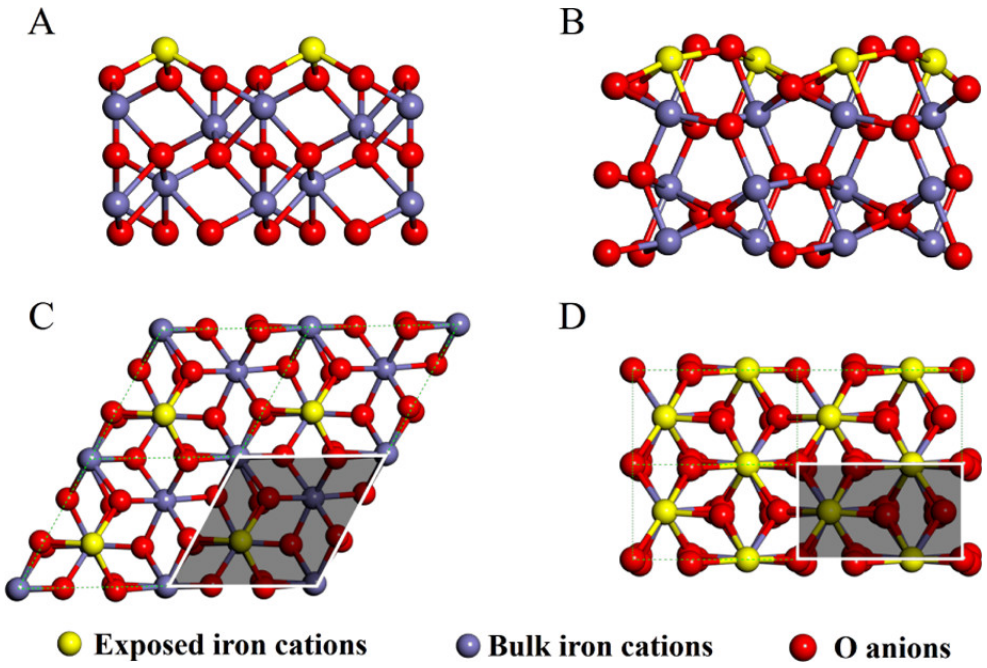


Figure 2. Atomic configuration and site density regulation on specific hematite facets. (**A**,**C**) Side and top views of the stoichiometric (001) facet, and (**B**,**D**) side and top views of the (012) facet. Yellow spheres represent coordination-unsaturated surface iron sites, while blue and red spheres denote bulk iron and oxygen atoms, respectively. The specific atomic arrangement determines the density and coordination state of active sites, directly impacting the energetic span of H_2O_2 activation. Reproduced with permission from Ref. [120], Copyright (2019) American Chemical Society.

3.3.2. Electronic Structure and Charge Transport Mechanisms

In the microkinetics of heterogeneous Fenton reactions, electron transfer serves as the central driving force for H_2O_2 activation and O-O bond cleavage. The regulation of Fenton performance by phase structure is fundamentally achieved through changes in the surface electron density, the thermodynamic barrier for Fe(III) reduction, the selectivity of electron-transfer pathways, and the efficiency of bulk charge transport. Since the reduction in Fe(III) to Fe(II) typically constitutes the kinetic bottleneck in the Fenton cycle, the intrinsic density of Fe(II) within the phase structure directly dictates the initial reaction rate. Zhong et al. (2017) [123] elucidated this structure-activity relationship in their study on the facet effect of magnetite (Fe_3O_4): compared to (100) and (110) facets, the (111) facet of magnetite crystallographically tends to terminate in Fe(II)-rich octahedral sites, as reflected in the facet-dependent activity map (Figure 3a,b). This high density of surface Fe(II) acts as an intrinsic electron donor, enabling H_2O_2 to undergo rapid single-electron reduction to generate $HO^{\bullet}$, thereby eliminating the reduction induction period [123]. For hematite (α-Fe_2O_3), which intrinsically lacks Fe(II), Wu et al. (2023) [124] demonstrated that specific

micromorphologies (such as leaf-like structures) can stabilize a higher proportion of surface Fe(II) species as a result of differences in crystal growth kinetics. This morphology-induced surface valence reconstruction directly accelerates the Fe(III)/Fe(II) redox cycle, establishing a positive correlation between surface electron density and macroscopic reaction rates [124].

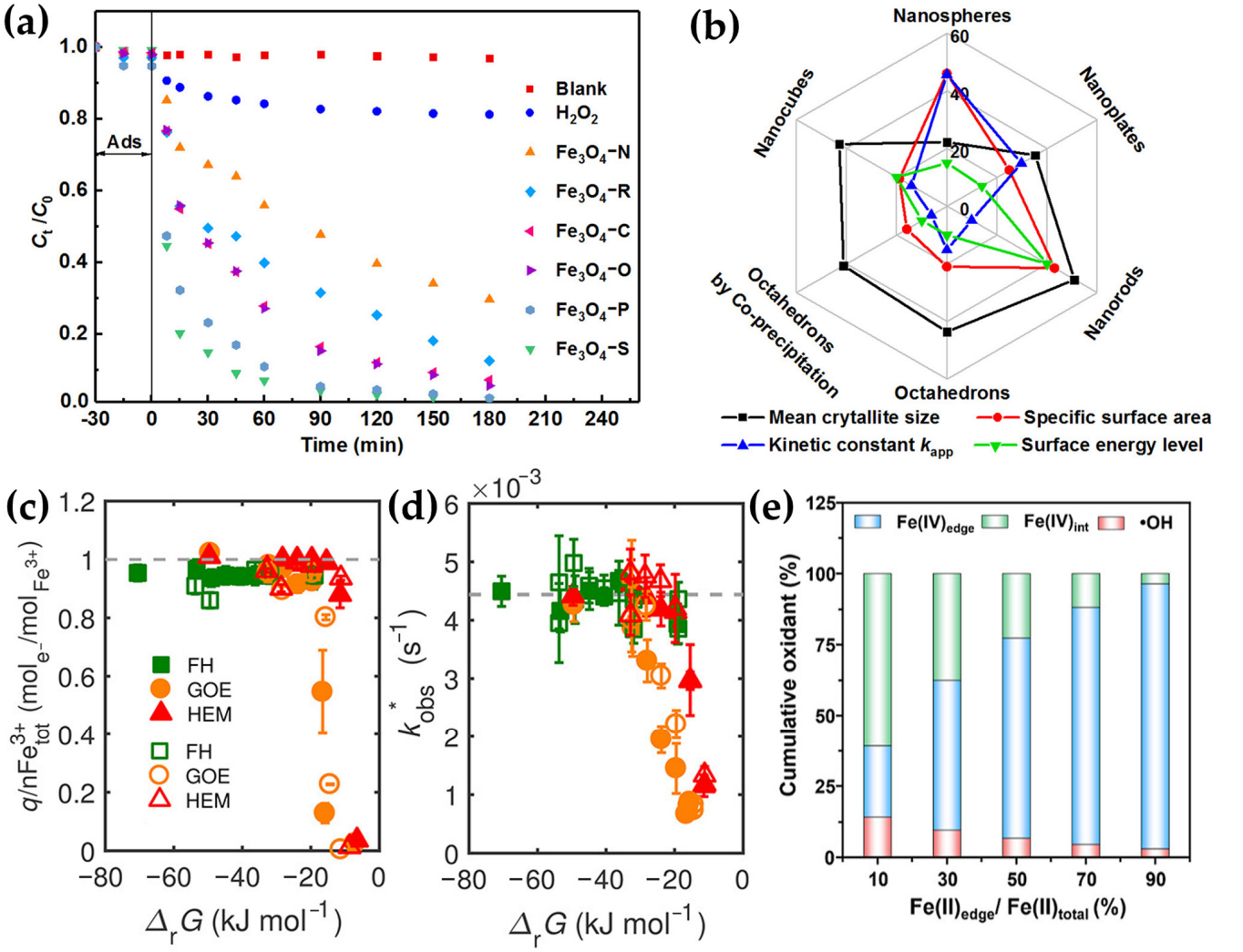


Figure 3. Electronic structure and local coordination environment governing reaction kinetics and selectivity. (**a**,**b**) Correlation between facet-dependent surface properties and Fenton-like activity of magnetite nanocrystals. The radar chart illustrates that facets exposing a higher density of active surface Fe(II) (e.g., (111) facets) exhibit superior catalytic rates (k_{app}). Reproduced from Ref. [123], Copyright (2017), with permission from American Chemistry Society. (**c**,**d**) Thermodynamic control over iron oxide reducibility determined by Mediated Electrochemical Reduction (MER). The data reveal linear free energy relationships (LFERs), demonstrating that the higher lattice stability of crystalline oxides imposes a larger energetic barrier for electron transfer compared to metastable ferrihydrite. k^*_{obs} denotes the corrected observed rate constant. Reproduced from Ref. [125], Copyright (2018), with permission from American Chemistry Society. (**e**) Kinetic modeling revealing the critical role of iron site location (edge vs. interior) on oxidant yields. The ratio of edge-surface Fe(II) determines the selectivity between single-electron transfer (generating HO•) and two-electron transfer (generating Fe(IV)). Reproduced from Ref. [126], Copyright (2024), with permission from American Chemistry Society.

Beyond the mere abundance of surface electron sources, the electron acceptance capability of Fe(III) sites constitutes another critical electronic-structure parameter governing Fenton cycle efficiency. In the rate-determining step of catalytic H_2O_2 decomposition, Fe(III)

must accept an electron to be reduced to catalytically active Fe(II). Aeppli et al. (2018) [125] employed electrochemical analysis to elucidate the role of lattice energy levels in this process: the reduction potential of iron oxides is significantly correlated with the electronic binding energy of the bulk lattice. Compared to highly crystalline, electronically stable phases like goethite or hematite, metastable ferrihydrite possesses higher Gibbs free energy and weaker Fe-O bond strength, which significantly lowers the energy barrier for electron injection into the Fe(III) antibonding orbitals (Figure 3c,d) [62]. This inherent feature of the electronic structure directly accelerates the regeneration rate of Fe(II), thereby overcoming the kinetic bottleneck of H_2O_2 activation in the Haber-Weiss cycle and establishing the intrinsic advantage of metastable phases in electron transfer dynamics.

However, the occurrence of electron transfer does not guarantee the generation of reactive radicals; the microscopic coordination environment of Fe(II) profoundly influences the selectivity of the electron transfer pathway. Yu et al. (2024) [126], in their investigation of the oxygenation process in iron-bearing minerals, demonstrated that Fe(II) located at the surface edge exhibits markedly different reactivity compared to Fe(II) located in the bulk lattice (Figure 3e). Experimental and modeling results confirmed that Fe(II) at edge sites preferentially drives a two-electron transfer process, leading to the formation of non-radical high-valent iron species (Fe(IV)) rather than $HO^{\bullet}$ via single-electron transfer. This mechanism indicates that specific coordination environments can divert electron transfer toward a less productive Fe(IV)-forming pathway, explaining the phenomenon where certain Fe(II)-rich minerals still exhibit low $HO^{\bullet}$ yields in practical reactions. This reveals the review-style summarizing sentence by which phase structure determines reaction pathway selectivity by regulating the spatial distribution of Fe(II).

Furthermore, in photo-assisted Fenton systems, the efficiency of electron excitation in the bulk and subsequent transport to the surface constitutes another limiting factor. If charge transport is hindered, photogenerated carriers are prone to recombination within the bulk, depriving surface active sites of the electrons required for reduction. Chen et al. (2025) [127] elucidated the role of crystallographic anisotropy in charge transport through DFT calculations and photoelectrochemical characterization. The study indicated that, although the hematite (104) facet possesses a stronger substrate adsorption capacity, the (116) facet provides a preferential channel for electron migration from the bulk to the surface due to its smaller effective electron mass and more favorable band bending. This favorable band structure significantly suppresses bulk electron-hole recombination, allowing a greater number of photogenerated electrons to reach the surface and participate in the in situ reduction in Fe(III).

In summary, the electronic properties derived from the phase structure represent a key factor underlying the observed disparities in H_2O_2 decomposition efficiency and reaction pathways. The surface Fe(II) electron supply density dictates the initial reaction kinetics, the electron acceptance capability of Fe(III) governs the turnover frequency of the catalytic cycle, whereas the local coordination environment and charge transport efficiency jointly regulate product selectivity and quantum efficiency, respectively. It is these electronic-level distinctions that largely determine whether H_2O_2 is converted into highly reactive species or undergoes futile consumption.

3.3.3. Interfacial Micro-Environment and Ligand Interaction

Although crystal structure and electronic properties define the intrinsic catalytic potential of iron (oxyhydr)oxides, Fenton reactions occur at the solid–liquid interface, where catalytic efficiency is ultimately governed by the local micro-environment. The phase structure therefore exerts a profoundly influences on the adsorption configuration

and activation pathway of H_2O_2 by determing the nature of surface hydroxyl groups, ligand coordination geometry, and the interfacial electric field.

Surface hydroxyl groups function as the primary binding sites for H_2O_2 via ligand exchange mechanisms, and their density and electronic configuration are critical determinants of the reaction pathway. Al-Ahmari et al. demonstrated that goethite possesses a significantly higher density of reactive hydroxyl species than hematite, which directly correlates with an enhanced capacity for oxidant adsorption. Beyond site density, the surface coverage and electronic nature of these hydroxyls modulate the stability of the precursor complex [128]. Chen et al. (2025) [129] elucidated how the specific coverage of terminal hydroxyls on the FeOCl (021) facet dictates the energetic span of H_2O_2 activation. Their DFT calculations demonstrated that a specific local chemical state, such as 50% terminal hydroxyl coverage, significantly lowers the energetic barrier for O–O bond cleavage compared to pristine or fully hydroxylated surfaces (Figure 4c,d). This indicates that the surface state stabilizes the adsorbate in a configuration that energetically favors reactive oxygen species generation over desorption [129].

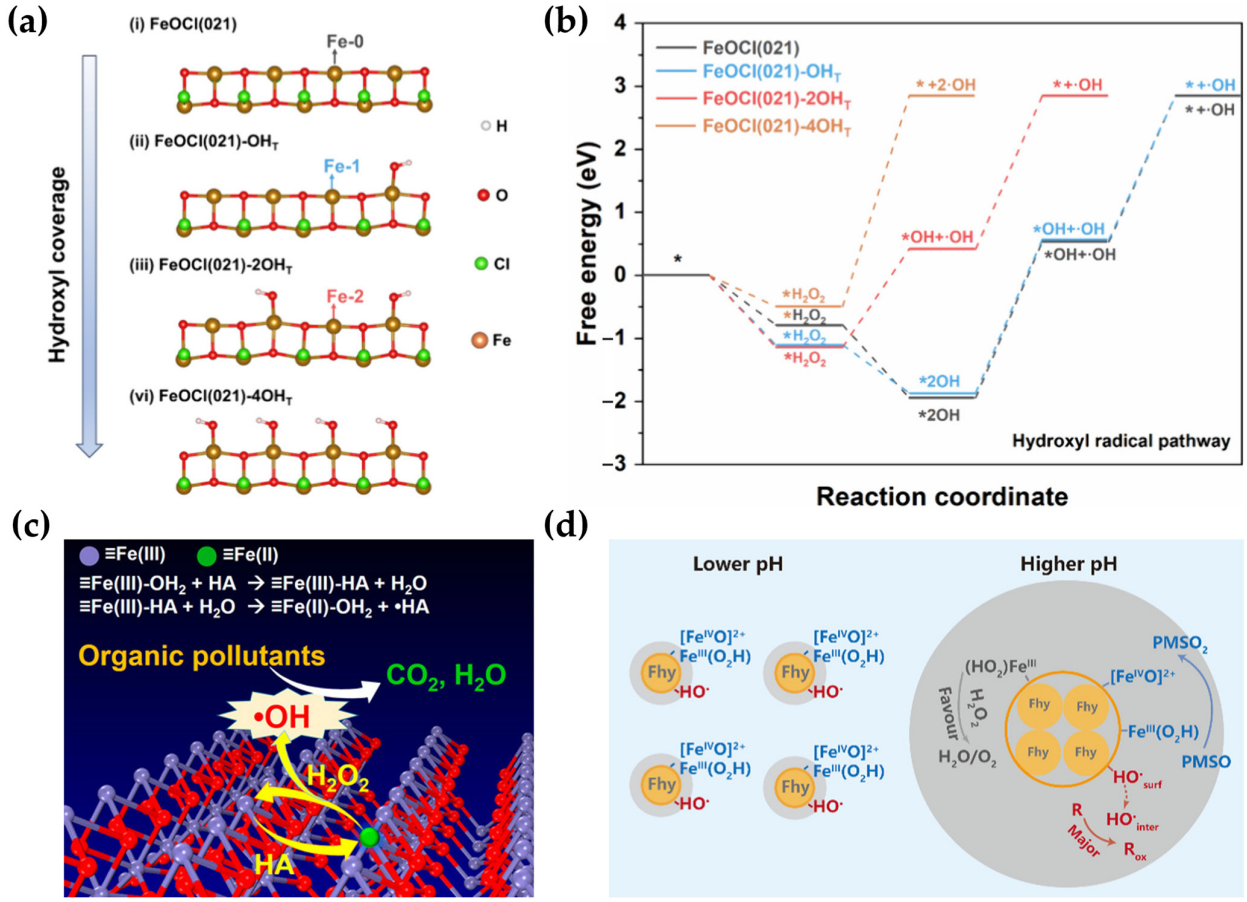


Figure 4. Regulation of H_2O_2 activation via interfacial micro-environment engineering. (**a**) Structural models of FeOCl (021) surfaces with varying terminal hydroxyl coverage and (**b**) corresponding calculated free energy profiles for the hydroxyl radical pathway, illustrating the impact of local chemical states on activation barriers. Reproduced with permission from Ref. [129]. (**c**) Schematic illustration of the hydroxylamine (HA) promoted surface Fenton mechanism on goethite, highlighting the acceleration of iron cycling through inner-sphere complexation. Reproduced with permission from Ref. [130]. (**d**) Schematic of pH-dependent reaction mechanisms, where lower pH favors particle dispersion and radical generation, whereas higher pH promotes non-radical pathways or inefficient decay. Reproduced with permission from Ref. [102]. Copyright American Chemical Society.

The coordination environment of surface iron species, distinct from the bulk phase, further regulates the activation energy barrier. This intrinsic reactivity can be restructured by coexisting ligands through ligand-to-metal charge transfer mechanisms. Hou et al. (2017) [130] demonstrated that the addition of reducing ligands such as hydroxylamine (HA) significantly enhances the catalytic performance of goethite by promoting a highly efficient surface ≡Fe(III)/≡Fe(II) cycle (Figure 4c). HA serves as a potent ligand that forms stable inner-sphere complexes, triggering rapid electron transfer to the ferric center [130]. This ligand-promoted pathway effectively bypasses the kinetic bottleneck of the traditional Haber-Weiss cycle without inducing significant iron leaching. Nevertheless, ligand interaction involves a complex trade-off mechanism, as noted by Huang et al., where strong coordination may passivate specific iron sites while simultaneously activating adjacent metal centers through electronic induction [131].

The interfacial electrostatic environment is fundamentally determined by the relationship between the solution pH and the catalyst point of zero charge. This relationship controls the surface protonation state, which in turn regulates the transition between inner-sphere and outer-sphere adsorption modes. As illustrated by Chen et al. (2022), the solution pH dictates the transition between different reaction pathways by modulating particle stability and protonation states (Figure 4d) [102]. Lower pH conditions support particle dispersion and the production of $HO^{\bullet}$. In contrast, higher pH leads to particle aggregation, which reduces the availability of active sites and promotes non-radical pathways or the inefficient decay of H_2O_2, highlighting the decisive role of the electrostatic micro-environment in determining the overall reaction selectivity.

3.4. Mechanistic Implications for Catalytic Performance and Stability

The structure–activity relationships and reactive species generation pathways delineated in the preceding sections (and summarized in Table 3) primarily reflect the catalytic behavior of iron (oxyhydr)oxides in their initial state. For practical implementation, however, the dynamic evolution of the catalyst under operational conditions and the resulting long-term performance are critical considerations that extend directly from the underlying mechanisms.

First, the high initial activity of certain phases is intrinsically linked to their thermodynamic metastability, making them prone to phase transformation or surface reconstruction during reaction. For instance, the structural Fe(II) on the magnetite (Fe_3O_4) surface, which is key to its superior activity, can be gradually oxidized during prolonged operation, potentially forming a less reactive maghemite (γ-Fe_2O_3)-like passivation layer and leading to activity decay [114]. Similarly, metastable ferrihydrite can transform into more crystalline phases like goethite or hematite via dissolution-reprecipitation pathways, particularly in the presence of aqueous Fe(II), drastically altering its surface area, porosity, and active site density [132]. Second, from a perspective of sustained efficiency and catalyst longevity, a phase exhibiting high initial activity is not necessarily optimal. Studies indicate that rapid H_2O_2 decomposition does not always correlate with efficient pollutant degradation. Some metastable minerals (e.g., ferrihydrite, feroxyhyte) decompose H_2O_2 swiftly but predominantly through non-productive pathways yielding O_2, contributing minimally to $HO^{\bullet}$ generation and resulting in low H_2O_2 utilization efficiency [87,133]. In contrast, thermodynamically more stable phases like hematite (α-Fe_2O_3) and goethite (α-FeOOH), although often exhibiting slower initial kinetics, tend to favor $HO^{\bullet}$ production and demonstrate greater structural durability over extended reaction periods [53,87].

Consequently, the evaluation of an iron (oxyhydr)oxide phase for a given application must strategically balance its inherent activity against its long-term structural stability and H_2O_2 utilization efficiency [15].

4. Strategies to Enhance the Performance of Iron (Oxyhydr)oxide/H_2O_2 Systems

The catalytic performance of iron (oxyhydr)oxides in heterogeneous Fenton systems can be constrained by various thermodynamic and kinetic limitations intrinsic to the solid–liquid interface. To overcome these challenges, recent efforts have primarily focused on structural design, defect engineering, and integration with functional substrates or through composite formation.

4.1. Precision Synthesis and Morphology Engineering

The efficiency of H_2O_2 utilization in heterogeneous Fenton systems is commonly constrained by the accessibility of active sites and the kinetics of interfacial electron transfer. Consequently, precision synthesis strategies have been developed not merely to tune catalysts' morphology, but to optimize the interaction between the oxidant and the mineral surface. Controlled wet-chemical methods, such as hydrothermal and solvothermal treatments, allow for the selective stabilization of high-energy crystal facets, which directly influence the adsorption configuration of H_2O_2. For instance, Wang et al. demonstrated that by manipulating the hydrothermal growth kinetics of α-Fe_2O_3, the exposure of specific atomic planes could be regulated. This crystallographic tailoring optimized the density of surface iron atoms, thereby enhancing the collision probability between H_2O_2. and the catalyst, leading to significantly improved photo-Fenton activity compared to non-oriented particles [118].

Beyond surface atomics, the construction of hierarchical and porous architectures via template-assisted synthesis addresses the challenge of mass transfer limitations, ensuring that H_2O_2 can efficiently reach internal active sites. Xie et al. fabricated three-dimensionally ordered macroporous (3DOM) iron oxide films using colloidal crystal templates. The resulting interconnected porous network not only facilitated the rapid diffusion of H_2O_2 into the bulk structure but also enhanced light harvesting, leading to a substantial increase in the generation rate of reactive oxygen species [134]. Building on this template strategy, Lu et al. demonstrated that the controlled pyrolysis of MIL-100(Fe) and polyaniline can generate mesoporous Fe_2O_3/N–C composites (Figure 5a) [135]. In this synthesis, the MIL-100(Fe) precursor serves as a self-sacrificing template that defines the initial porous framework, while the PANI coating acts as a secondary carbon and nitrogen source. During the thermal treatment, the decomposition of organic ligands and the carbonization of PANI release gaseous byproducts, preventing the collapse of the pore structure. This strategy stabilizes iron nanocrystals within a mesoporous nitrogen-doped framework, significantly enhancing the collision probability between H_2O_2 and the catalyst surface. Innovative precipitation techniques, such as the plasma-assisted approach introduced by Tiya-Djowe et al., further demonstrate that non-equilibrium synthesis can achieve highly dispersed iron species on supports. Such high dispersion effectively prevents the agglomeration of active phases, maximizing the specific activity per unit mass of iron and reducing the futile self-decomposition of H_2O_2 that often occurs on bulk oxide surfaces [136].

A further evolution of morphology engineering involves the dynamic reconstruction of the MOF architecture. Bondarenko et al. (2024) reported that the chemical modification of MIL-88B(Fe) can induce a drastic morphological shift from traditional bipyramidal prisms to a layered structure (Figure 5b) [137]. This morphological engineering not only increases the accessible surface area but also facilitates the Fe^{3+}/Fe^{2+} redox turnover at the interface. As quantitatively shown in Figure 5c, this structural optimization leads to a significantly higher reaction rate constant (k) compared to unmodified iron oxides or pure MOFs, highlighting the critical role of precise morphological control in overcoming the kinetic bottlenecks of H_2O_2 activation.

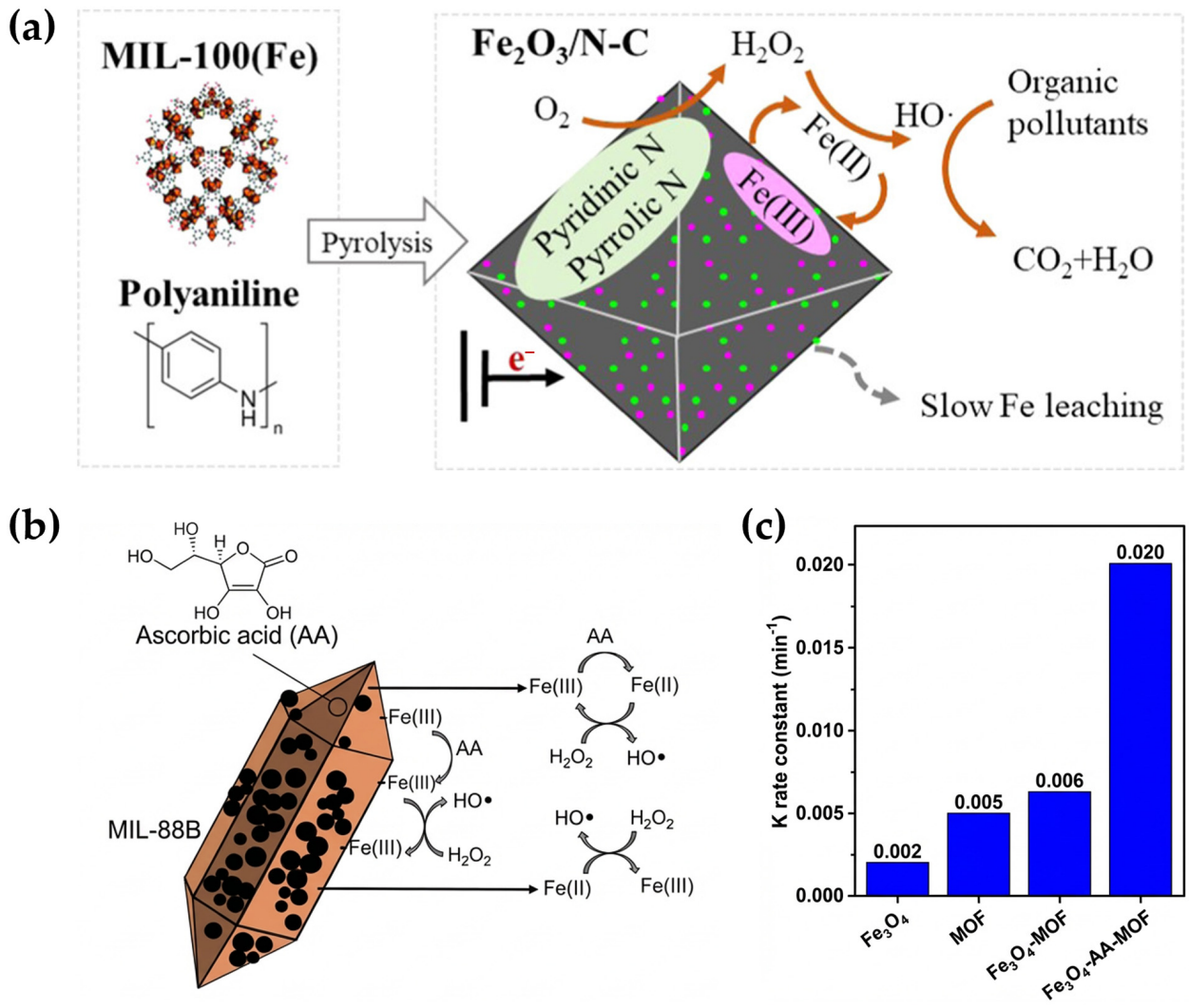


Figure 5. Precision engineering of active sites and morphological evolution via synthesis strategies. (**a**) Schematic illustration of the topotactic transformation from MIL-100(Fe)/PANI precursors to Fe_2O_3/N–C composites, optimizing the distribution of active iron species within a porous nitrogen-doped carbon matrix. The pink and green dots correspond to iron oxide and N-doped sites, respectively. Reproduced with permission from Ref. [135], Copyright (2020), American Chemical Society. (**b**) Morphological and structural evolution of MIL-88B(Fe) following precise chemical modification, showing the transition from bipyramidal prisms to a layered architecture. (**c**) Quantitative evaluation of Fenton-like reaction rate constants (*k*) for different iron-based catalysts, demonstrating the kinetic advantages of morphology-engineered MOF composites. Reproduced with permission from Ref. [137], Copyright (2024), Royal Society of Chemistry.

4.2. Defect Engineering and Heteroatom Doping

Lattice engineering, primarily through defect construction and heteroatom doping, is employed to overcome the intrinsic limitations of iron (oxyhydr)oxides. Specifically, the introduction of oxygen vacancies (OVs) has been widely adopted as an effective modification strategy. For instance, Jin et al. employed a Cu-substitution strategy to engineer magnetic Fe_3O_4@FeOOH nanocomposites, where the substitution of Fe species generated abundant surface oxygen vacancies [138] (Figure 6). These doping-induced vacancies functioned as electron-rich active centers that significantly lowered the adsorption energy of H_2O_2, accelerating its activation by 12.3 times compared to the pristine counterpart. Notably, this defect-rich structure enabled robust catalytic performance across a broad pH range (3.2–9.0), effectively mitigating the acidic constraints typical of heterogeneous Fenton systems.

Defect engineering strategies have also been extended to photo-assisted Fenton systems. Wu et al. constructed oxygen vacancy-rich α-FeOOH anchored on reduced graphene oxide (rGO) to address the issue of rapid electron-hole recombination [139]. In this system, the engineered surface oxygen vacancies functioned as charge capture centers. These defects effectively inhibited the recombination of electrons and holes, thereby facilitating the transfer of photogenerated electrons to surface Fe(III) sites for improved redox cycling. This vacancy-mediated mechanism resulted in a 3.6-fold enhancement in visible-light-driven activity.

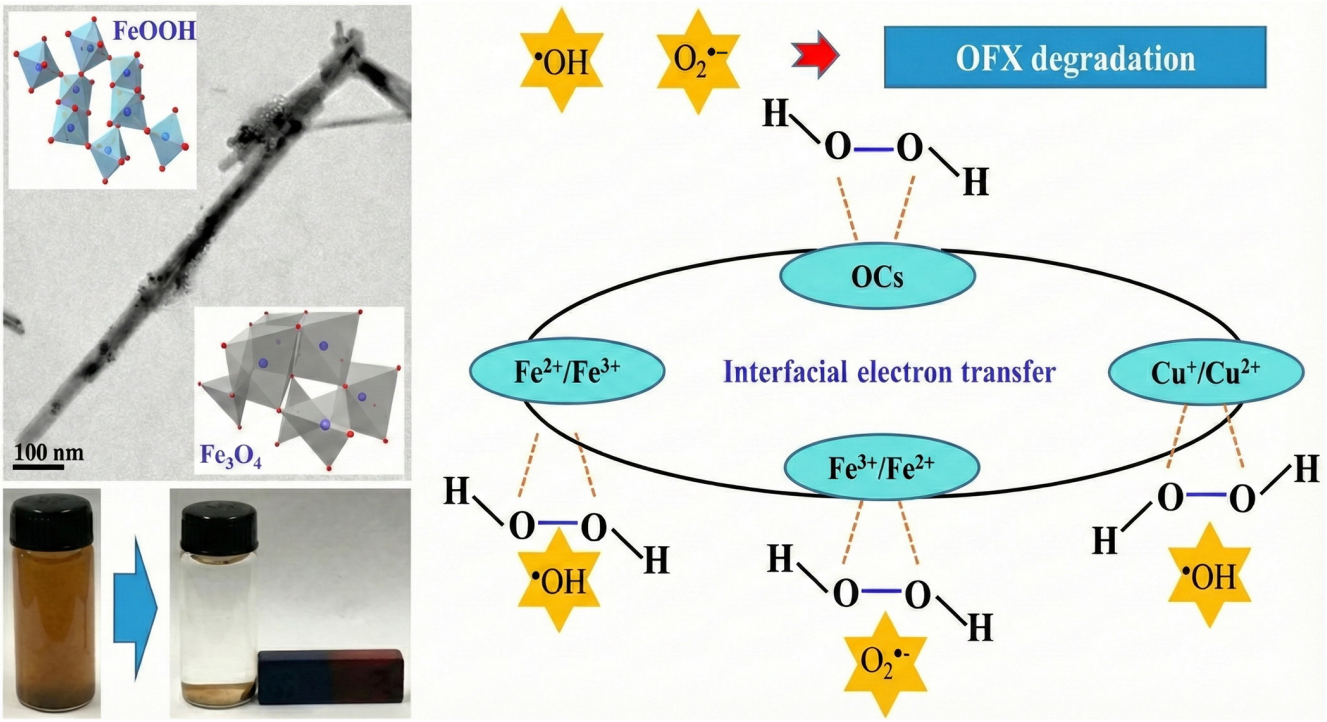


Figure 6. Enhanced photo-Fenton performance via heteroatom doping: Synthesis route, elemental characterization, and visible-light-driven catalytic activity of Zn-doped Fe_3O_4. Reproduced with permission from Ref. [138], Copyright (2017), American Chemical Society.

Furthermore, defect engineering is also applied to regulate oxidant consumption behaviors. Chen et al. developed a Ti-doped Mn_3O_4/Fe_3O_4 ternary catalyst where heteroatom doping induced surface defects that facilitated an O_2-activation mechanism [140]. Specifically, the oxygen vacancies mediated a redox cycle involving the capture and activation of evolved O_2 to regenerate H_2O_2. This in situ regeneration strategy minimized the waste of oxidants into oxygen gas, achieving a high H_2O_2 utilization efficiency where the consumed oxidant was maximally converted into effective degradation capability.

Heteroatom doping, encompassing both metal and non-metal incorporation, is also widely employed to optimize the overall reaction efficiency of iron (oxyhydr)oxides. For example, Li et al. developed a Mn-doped FeOOH catalyst supported on carbonized aerogel (CA) [141]. In this system, the Mn dopant played a critical role in accelerating the regeneration of Fe^{2+}, while the high-porosity CA served as an electron transport channel. The synergy between Mn-doping and the conductive support facilitated efficient electron transfer, significantly promoting the decomposition of H_2O_2 into $HO^{\bullet}$ and solving the mass transfer limitations typical of traditional heterogeneous systems.

Heteroatom doping is also effective in enhancing the performance of photo-assisted Fenton processes. Li et al. prepared an Ag-doped FeOOH film that exhibited distinct visible-light responsiveness, achieving a 93.2% pollutant removal efficiency due to the significantly enhanced photo-Fenton activity [142]. Beyond noble metals, transition metal

doping has also been investigated. Xu et al. reported that Cu-doped α-FeOOH surpassed its pristine counterpart in photo-Fenton activity, attributing the enhancement to Cu(I) species that not only activated H_2O_2 but also facilitated the reduction in Fe(III) to Fe(II) [143]. Furthermore, Nguyen et al. synthesized Zn-doped Fe_3O_4 (Figure 7) and found that the Zn dopant accelerated electron transfer between Fe(III) and H_2O_2, ensuring high and stable degradation performance under visible light irradiation [144].

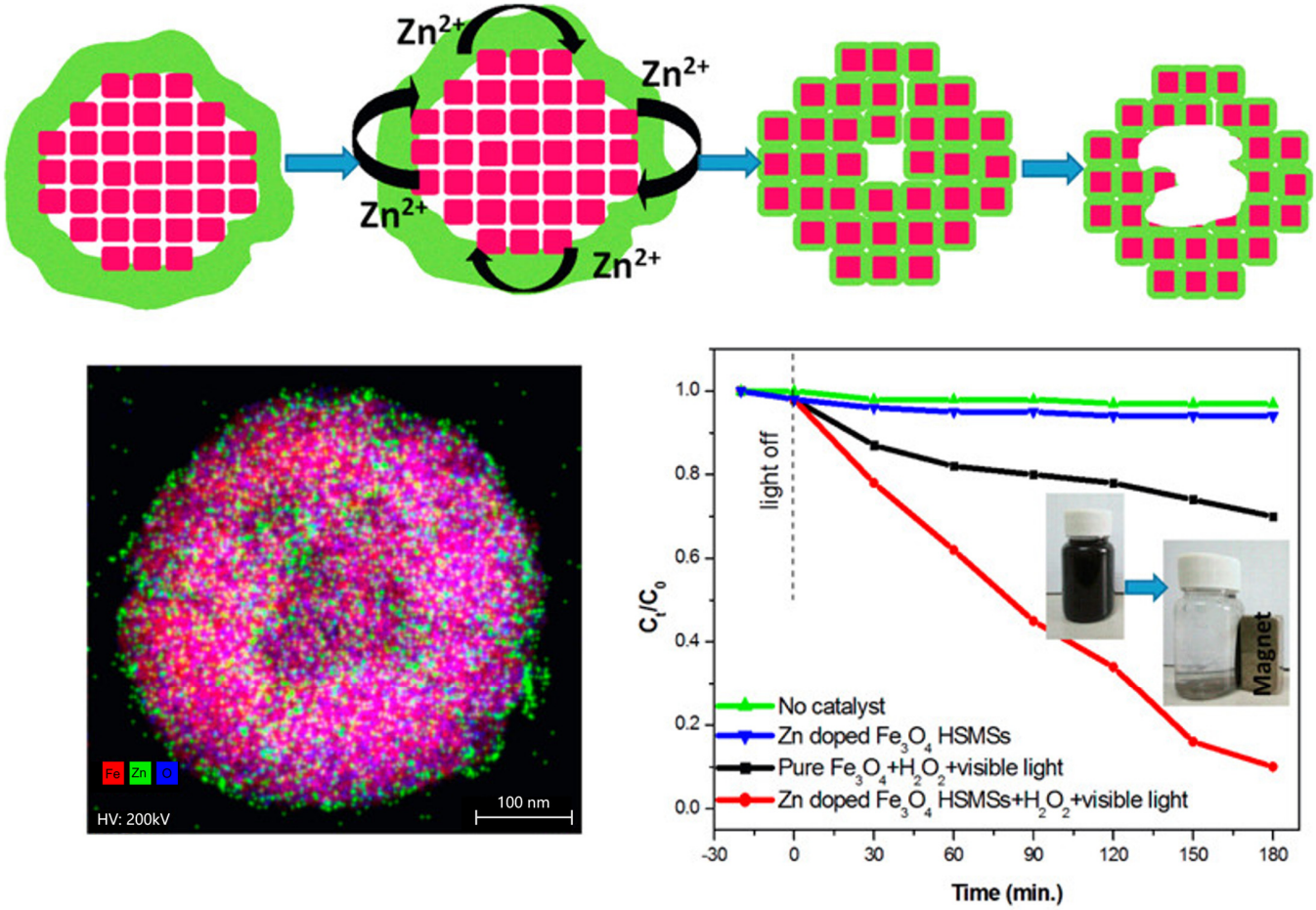


Figure 7. Synthesis, elemental characterization, and visible-light-driven photo-Fenton performance of Zn-doped Fe_3O_4 nanoparticles. Reproduced with permission from Ref. [144], Copyright (2017), American Chemical Society.

Currently, co-doping strategies are also employed to achieve multi-functional optimization. Sun et al. synthesized a Cu/Ti co-doped Fe_3O_4@FeOOH catalyst, where surface Cu(I) species facilitated interfacial electron transfer to boost catalytic activity, while Ti doping into the lattice significantly enhanced the magnetic properties and structural stability [145]. This dual-doping approach not only broadened the operational pH range (6.5–12.5) but also modulated the reactive species, generating both HO$^{\bullet}$ and Fe(IV) to adapt to different acid-base conditions.

Furthermore, studies have shown that non-metal modification can alter the reaction pathway. Tian et al. revealed that surface sulfidation of β-FeOOH (Fe_3S_4@β-FeOOH) introduced sulfur species (S^{2-}, S^0, and S_n^{2-}) that acted as electron donors and shuttles (Figure 8) [146]. This configuration enabled the efficient conversion of Fe(III) into Fe(II) via a mechanism distinct from the conventional Haber–Weiss cycle. Consequently, this modification not only enhanced HO$^{\bullet}$ formation but also generated sulfate radicals ($SO_4^{\bullet-}$)

as new oxidation species via the conversion of sulfite intermediates, providing a novel route to improve oxidant utilization.

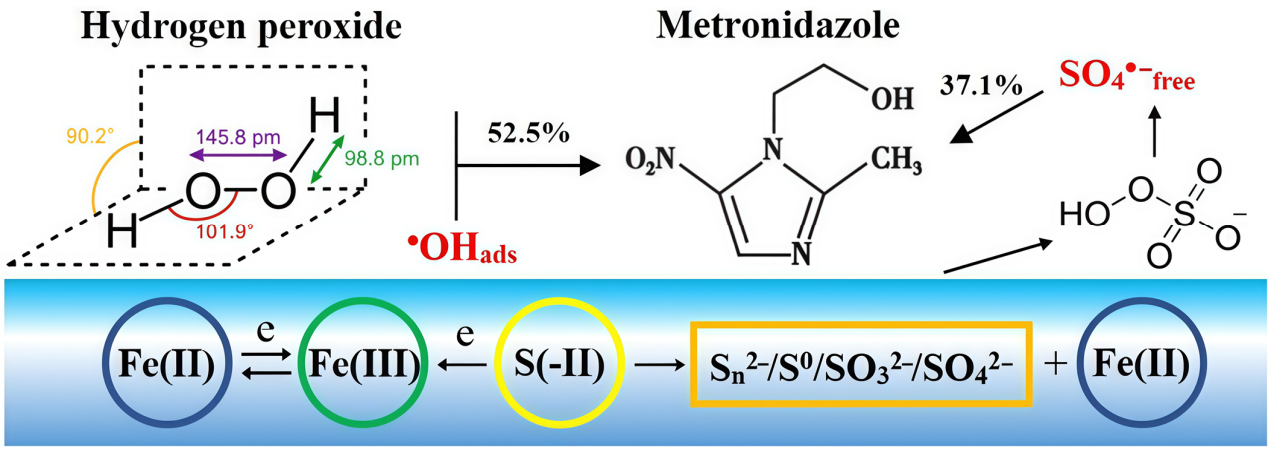


Figure 8. Proposed mechanism for sulfur species-mediated Fe(III)/Fe(II) cycling and radical generation in sulfidated β-FeOOH systems. Reproduced with permission from Ref. [146], Copyright (2022), American Chemical Society.

4.3. Interface Construction and Composite Systems

Single-phase iron (oxyhydr)oxide catalysts frequently suffer from intrinsic limitations such as low electrical conductivity, particle agglomeration, and rapid charge carrier recombination in photo-assisted processes. To address these macroscopic kinetic barriers, the construction of heterogeneous interfaces has emerged as a strategy for optimizing charge transport pathways and the spatial distribution of active species.

Integrating iron-based active phases with conductive substrates enhances interfacial electron transfer. Carbonaceous materials can function as effective electron acceptors and transport channels. Qian et al. fabricated a visible-light-driven α-FeOOH/mesoporous carbon composite via in situ crystallization. In this architecture, the strong C-O-Fe interfacial bonds formed between the FeOOH nanocrystals and the carbon matrix served as efficient electron transport channels, which not only inhibited iron leaching but also accelerated the rate-limiting Fe(III)/Fe(II) cycle [147]. The electron transfer and catalytic mechanism within this composite interface are illustrated in Figure 9. Similarly, Su et al. demonstrated that β-FeOOH nanorods grown on graphene oxide form specific Fe-O-C interfacial bonds. These interfacial linkages anchor the catalyst, facilitating the transfer of photogenerated electrons to surface Fe(III) sites for regeneration [148].

A specific advancement in interfacial engineering involves the regulation of reactant concentrations through framework design. Xiaoping Wang et al. (2020) [149] synthesized a Fe_3O_4 zeolite cyclodextrin composite to control the utilization of H_2O_2 (Figure 10a). The cyclodextrin at the solid–liquid interface captures H_2O_2 and facilitates its gradual desorption at the active sites. This interfacial regulation prevents the rapid and unproductive decomposition of the oxidant and enhances the efficiency of wastewater treatment [149]. The synergy between FeOOH QDs and the Z-scheme heterojunction effectively promoted charge separation and iron cycling, leading to superior photo-Fenton activity [150]. The mechanisms of H_2O_2 release regulation and enhanced charge carrier migration in these composite systems are schematically shown in Figure 10.

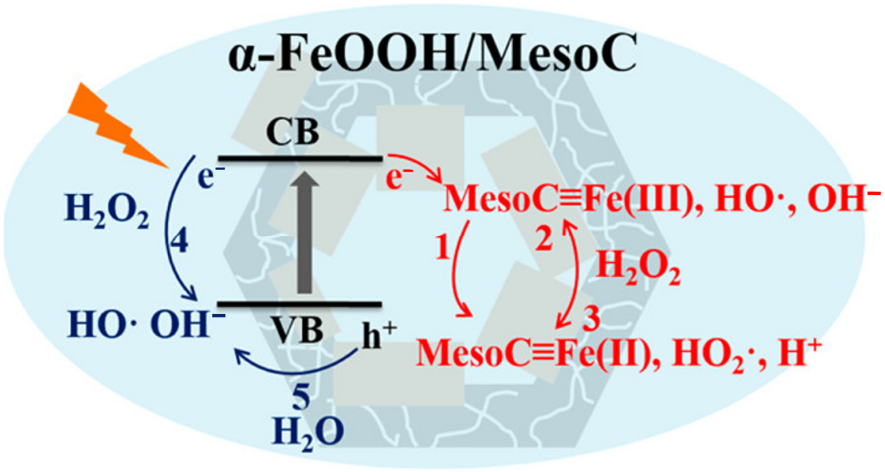


Figure 9. Electron transfer and catalytic mechanism within the visible-light-driven α-FeOOH/mesoporous carbon composite interface. Reproduced with permission from Ref. [147], Copyright (2017), American Chemical Society.

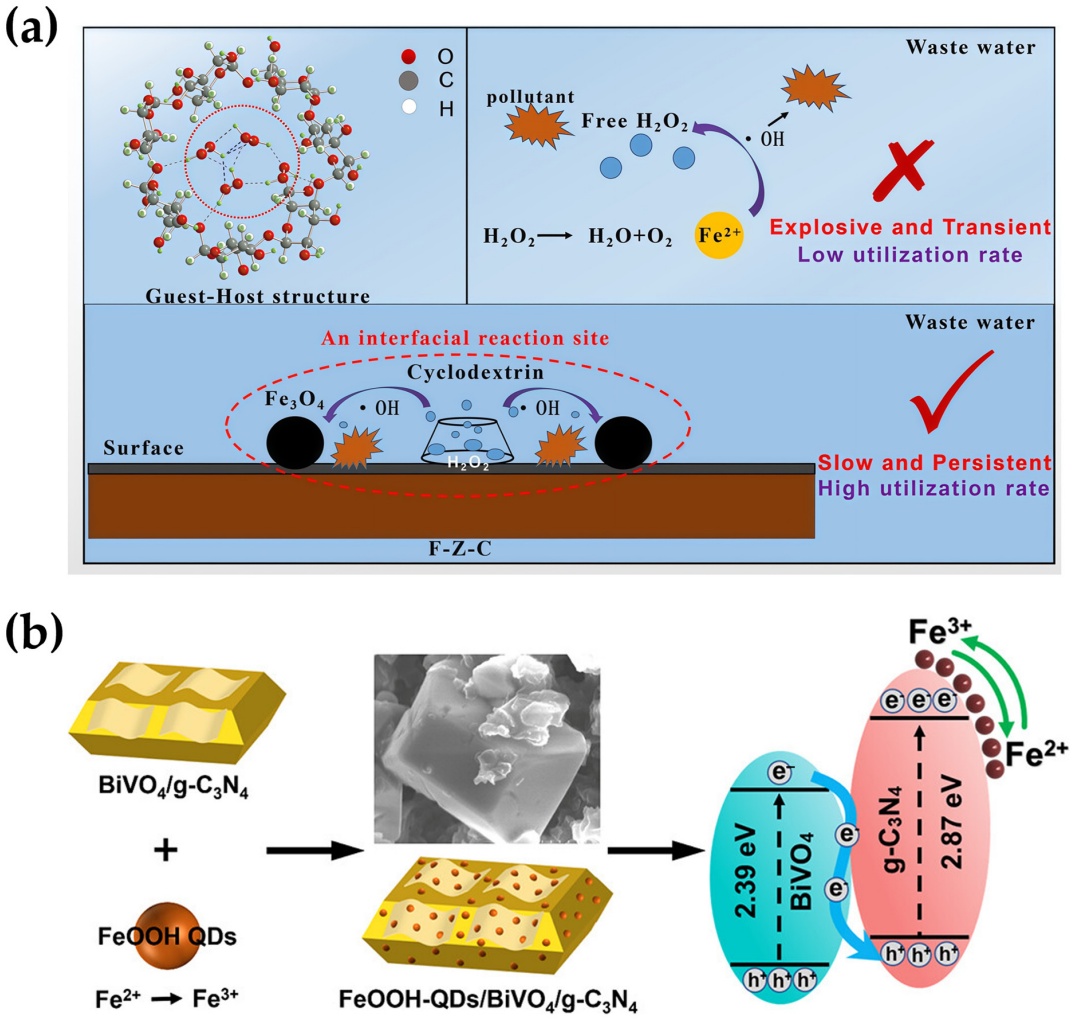


Figure 10. (**a**) Mechanism of sustained H_2O_2 release regulated by the Fe_3O_4-zeolite-cyclodextrin composite interface. Reproduced with permission from Ref. [149], Copyright (2020), American Chemical Society. (**b**) Charge carrier migration and enhanced iron cycling in a FeOOH quantum dot-coupled Z-scheme $BiVO_4$/g-C_3N_4 heterojunction. Reproduced with permission from Ref. [150], Copyright (2023), American Chemical Society.

While these optimization strategies have demonstrated significant potential in laboratory settings, their translation to practical applications faces several challenges. Precise morphology control and defect engineering often require complex, energy-intensive synthesis procedures (e.g., solvothermal or plasma treatments) that are difficult to scale up cost-effectively [10]. Furthermore, the stability of engineered active sites remains a concern; for instance, surface oxygen vacancies are thermodynamically metastable and may be gradually consumed by oxidation during the Fenton reaction, leading to activity decay over time [15,54]. Additionally, for heteroatom-doped catalysts, the potential leaching of toxic dopant metals poses a risk of secondary pollution, necessitating a rigorous evaluation of their long-term environmental safety before deployment [9,10].

5. Conclusions and Perspectives

This review systematically elucidates the structure-activity relationships of iron (oxyhydr)oxides in heterogeneous Fenton reactions. The crystal structure, electronic properties (e.g., band structure and charge transport capability), and surface chemistry of different minerals collectively form the physicochemical basis of their catalytic behavior. Under specific conditions, these intrinsic characteristics may influence the reaction efficiency and selectivity through various pathways, such as modulating H_2O_2 adsorption, the kinetics of the Fe(III)/Fe(II) cycle, and the generation pathways of reactive oxygen species (e.g., $HO^{\bullet}$, Fe(IV), or $^1O_2$). Recent performance enhancements achieved through morphology engineering, defect construction, and composite material design essentially reflect the synergistic regulation of these multiple intrinsic factors to enable more efficient H_2O_2 activation. Looking ahead, future research needs to further focus on two key challenges: the dynamic structural evolution of catalysts under realistic reaction conditions and the accurate identification of active intermediates. It is essential to integrate in situ characterization techniques with theoretical simulations to monitor the evolution of active sites in real time and clarify intermediate reaction pathways in complex aqueous matrices close to practical applications. At the same time, systematic evaluation of the interactions between actual water components and specific mineral surfaces will provide more precise and practical guidance for the design of iron-based Fenton catalysts with high activity, high selectivity, and long-term stability.

Author Contributions: Conceptualization, Y.W., Y.C. and D.W.; investigation, Y.W.; writing—original draft preparation, Y.W.; writing—review and editing, Y.C. and D.W.; supervision, Y.C. and D.W.; project administration, Y.C. and D.W.; funding acquisition, Y.C. and D.W. All authors have read and agreed to the published version of the manuscript.

Funding: This research was funded by the National Natural Science Foundation of China, grant numbers 52300110, 42377390 and 52170091.

Data Availability Statement: No new data were created or analyzed in this study. Data sharing is not applicable to this article.

Conflicts of Interest: The authors declare no conflicts of interest.

Abbreviations

The following abbreviations are used in this manuscript:

2,4-DCP	2,4-Dichlorophenol
3DOM	Three-Dimensionally Ordered Macroporous
4-HBA	4-Hydroxybenzoic Acid
AAO	Anodic Aluminum Oxide
AOPs	Advanced Oxidation Processes

ATZ	Atrazine
BA	Benzoic Acid
BET	Brunauer–Emmett–Teller
BSA	5-Bromosalicylic Acid
BuCl	Butyl Chloride
CA	Carbonized Aerogel
CNTs	Carbon Nanotubes
DEP	Diethyl Phthalate
DFT	Density Functional Theory
DMSO	Dimethyl Sulfoxide
ESR	Electron Spin Resonance
ET	Electron Transfer
Fe(IV)	Iron(IV)-oxo Species
FFA	Furfuryl Alcohol
H_2O_2	Hydrogen Peroxide
HCA	Hexachloroethane
$HO^{\bullet}$	Hydroxyl Radical
IEP	Isoelectric Point
MB	Methylene Blue
MNPs	Magnetic Nanoparticles
MOF	Metal–Organic Framework
NaN_3	Sodium Azide
NB	Nitrobenzene
NOM	Natural Organic Matter
OVs	Oxygen Vacancies
PAA	Phenylacetic Acid
PANI	Polyaniline
pCBA	para-Chlorobenzoic Acid
PMSO	Methyl Phenyl Sulfoxide
PZC	Point of Zero Charge
$^1O_2$	Singlet Oxygen
rGO	Reduced Graphene Oxide
ROS	Reactive Oxygen Species
XAS	X-ray Absorption Spectroscopy

References

1. Mantzavinos, D.; Petala, A.; Arvaniti, O.S. Advanced Catalytic Processes for Wastewater Treatment. *Catalysts* **2025**, *15*, 855. [CrossRef]
2. Xu, Y.; Wang, Q.; Yoza, B.A.; Li, Q.X.; Kou, Y.; Tang, Y.; Ye, H.; Li, Y.; Chen, C. Catalytic ozonation of recalcitrant organic chemicals in water using vanadium oxides loaded ZSM-5 zeolites. *Front. Chem.* **2019**, *7*, 384. [CrossRef] [PubMed]
3. Dong, C.; Fang, W.; Yi, Q.; Zhang, J. A comprehensive review on reactive oxygen species (ROS) in advanced oxidation processes (AOPs). *Chemosphere* **2022**, *308*, 136205. [CrossRef] [PubMed]
4. Hübner, U.; Spahr, S.; Lutze, H.; Wieland, A.; Rüting, S.; Gernjak, W.; Wenk, J. Advanced oxidation processes for water and wastewater treatment–Guidance for systematic future research. *Heliyon* **2024**, *10*, e30402. [CrossRef]
5. Feijoo, S.; Yu, X.; Kamali, M.; Appels, L.; Dewil, R. Generation of oxidative radicals by advanced oxidation processes (AOPs) in wastewater treatment: A mechanistic, environmental and economic review. *Rev. Environ. Sci. Bio/Technol.* **2023**, *22*, 205–248. [CrossRef]
6. Zhang, M.H.; Dong, H.; Zhao, L.; Wang, D.X.; Meng, D. A review on Fenton process for organic wastewater treatment based on optimization perspective. *Sci. Total Environ.* **2019**, *670*, 110–121. [CrossRef]
7. Lin, Y.M.; Qiao, J.L.; Sun, Y.K.; Dong, H.Y. The profound review of Fenton process: What's the next step? *J. Environ. Sci.* **2025**, *147*, 114–130. [CrossRef]
8. Ahmed, N.; Vione, D.; Rivoira, L.; Carena, L.; Castiglioni, M.; Bruzzoniti, M.C. A Review on the Degradation of Pollutants by Fenton-Like Systems Based on Zero-Valent Iron and Persulfate: Effects of Reduction Potentials, pH, and Anions Occurring in Waste Waters. *Molecules* **2021**, *26*, 4584. [CrossRef]

9. Nidheesh, P.V. Heterogeneous Fenton catalysts for the abatement of organic pollutants from aqueous solution: A review. *RSC Adv.* **2015**, *5*, 40552–40577. [CrossRef]
10. Thomas, N.; Dionysiou, D.D.; Pillai, S.C. Heterogeneous Fenton catalysts: A review of recent advances. *J. Hazard. Mater.* **2021**, *404*, 124082. [CrossRef]
11. Chen, Y.; Huang, N.; Li, Y.; Lu, Y.; Jiang, Y.; Zhou, Z.; Wang, D. Physical and chemical processes driven by natural iron minerals in aquatic environments. *Water Cycle* **2025**, *6*, 36–48. [CrossRef]
12. Jiménez-Vázquez, A.; Jaimes-López, R.; Morales-Bautista, C.M.; Pérez-Rodríguez, S.; Gochi-Ponce, Y.; Estudillo-Wong, L.A. Catalytic Applications of Natural Iron Oxides and Hydroxides: A Review. *Catalysts* **2025**, *15*, 236. [CrossRef]
13. Faivre, D. *Iron Oxides: From Nature to Applications*; John Wiley & Sons: Hoboken, NJ, USA, 2016.
14. Huang, J.; Jones, A.; Waite, T.D.; Chen, Y.; Huang, X.; Rosso, K.M.; Kappler, A.; Mansor, M.; Tratnyek, P.G.; Zhang, H. Fe (II) redox chemistry in the environment. *Chem. Rev.* **2021**, *121*, 8161–8233. [CrossRef] [PubMed]
15. He, J.; Yang, X.F.; Men, B.; Wang, D.S. Interfacial mechanisms of heterogeneous Fenton reactions catalyzed by iron-based materials: A review. *J. Environ. Sci.* **2016**, *39*, 97–109. [CrossRef] [PubMed]
16. Petigara, B.R.; Blough, N.V.; Mignerey, A.C. Mechanisms of hydrogen peroxide decomposition in soils. *Environ. Sci. Technol.* **2002**, *36*, 639–645. [CrossRef] [PubMed]
17. Li, F.; Li, J.; Gao, L.; Hu, Y.; Long, X.; Wei, S.; Wang, C.; Jin, J.; Ma, J. Construction of an efficient hole migration pathway on hematite for efficient photoelectrochemical water oxidation. *J. Mater. Chem. A* **2018**, *6*, 23478–23485. [CrossRef]
18. Fleet, M.E. The structure of magnetite. *Struct. Sci.* **1981**, *37*, 917–920. [CrossRef]
19. Cornell, R.M.; Schwertmann, U. *The Iron Oxides: Structure, Properties, Reactions, Occurrences and Uses*; John Wiley & Sons: Hoboken, NJ, USA, 2003.
20. Gualtieri, A.F.; Giacobbe, C.; Viti, C. The natural occurrence of asbestos-like magnetite fibers. *J. Hazard. Mater.* **2019**, *373*, 560–569.
21. Usman, M.; Byrne, J.M.; Chaudhary, A.; Orsetti, S.; Hanna, K.; Ruby, C.; Kappler, A.; Haderlein, S.B. Magnetite and Green Rust: Synthesis, Properties, and Environmental Applications of Mixed-Valent Iron Minerals. *Chem. Rev.* **2018**, *118*, 3251–3304. [CrossRef]
22. Wang, J.; Guo, H.; Wei, S.; Li, G. Heterogeneous Fenton degradation of bisphenol A catalyzed by efficient magnetic Fe_3O_4/GO nanocomposites. *Chem. Eng. J.* **2018**, *334*, 1886–1896.
23. Sepyani, F.; Soltani-Felehgari, F.; Maleki, A. Immobilization of magnetite nanoparticles on a metal-organic framework for the degradation of organic pollutants. *J. Clean. Prod.* **2018**, *203*, 1073–1083.
24. Skomurski, F.N.; Kerisit, S.; Rosso, K.M. Structure, charge distribution, and electron hopping dynamics in magnetite (Fe_3O_4)(1 0 0) surfaces from first principles. *Geochim. Cosmochim. Acta* **2010**, *74*, 4234–4248. [CrossRef]
25. Gorski, C.A.; Handler, R.M.; Beard, B.L.; Pasakarnis, T.; Johnson, C.M.; Scherer, M.M. Fe atom exchange between aqueous Fe^{2+} and magnetite. *Environ. Sci. Technol.* **2012**, *46*, 12399–12407. [CrossRef] [PubMed]
26. Gawande, M.B.; Branco, P.S.; Varma, R.S. Nano-magnetite (Fe_3O_4) as a support for recyclable catalysts in the development of sustainable methodologies. *Chem. Soc. Rev.* **2013**, *42*, 3371–3393. [CrossRef] [PubMed]
27. Liu, M.Y.; Ye, Y.Y.; Ye, J.M.; Gao, T.; Wang, D.H.; Chen, G.; Song, Z.J. Recent Advances of Magnetite (Fe_3O_4)-Based Magnetic Materials in Catalytic Applications. *Magnetochemistry* **2023**, *9*, 110. [CrossRef]
28. Lu, A.H.; Salabas, E.e.L.; Schüth, F. Magnetic nanoparticles: Synthesis, protection, functionalization, and application. *Angew. Chem. Int. Ed.* **2007**, *46*, 1222–1244. [CrossRef]
29. Eskandari, M.J.; Hasanzadeh, I. Size-controlled synthesis of Fe_3O_4 magnetic nanoparticles via an alternating magnetic field and ultrasonic-assisted chemical co-precipitation. *Mater. Sci. Eng. B* **2021**, *266*, 115050. [CrossRef]
30. Hu, Y.; Li, F.; Yuan, S.; Wang, Y.; Ai, Z. Facet-dependent Fenton-like catalysis of magnetite nanoprisms. *Appl. Catal. B Environ.* **2021**, *286*, 119856.
31. Parkinson, G.S. Iron oxide surfaces. *Surf. Sci. Rep.* **2016**, *71*, 272–365. [CrossRef]
32. Tombácz, E. pH-dependent surface charging of metal oxides. *Period. Polytech. Chem. Eng.* **2009**, *53*, 77–86. [CrossRef]
33. Mansour, C.; Lefèvre, G.; Pavageau, E.; Catalette, H.; Fédoroff, M.; Zanna, S. Sorption of sulfate ions onto magnetite. *J. Colloid Interface Sci.* **2009**, *331*, 77–82. [CrossRef]
34. Gao, L.; Zhuang, J.; Nie, L.; Zhang, J.; Zhang, Y.; Gu, N.; Wang, T.; Feng, J.; Yang, D.; Perrett, S. Intrinsic peroxidase-like activity of ferromagnetic nanoparticles. *Nat. Nanotechnol.* **2007**, *2*, 577–583. [CrossRef] [PubMed]
35. Shmakov, A.; Kryukova, G.; Tsybulya, S.; Chuvilin, A.; Solovyeva, L. Vacancy ordering in γ-Fe_2O_3: Synchrotron X-ray powder diffraction and high-resolution electron microscopy studies. *Appl. Crystallogr.* **1995**, *28*, 141–145. [CrossRef]
36. Bentarcurt, Y.; Calatayud, M.; Fernández-Sanz, J.; Klapp, J.; Ruette, F. Theoretical Study of Hydrogen Activation and Reduction of an Oxidized Maghemite Surface, γ-Fe_2O_3,(001) by Monovacancy Formation: An Analysis Using Density Functional Theory (DFT). *Surf. Sci.* **2025**, *765*, 122877. [CrossRef]

37. Laurent, S.; Forge, D.; Port, M.; Roch, A.; Robic, C.; Vander Elst, L.; Muller, R.N. Magnetic iron oxide nanoparticles: Synthesis, stabilization, vectorization, physicochemical characterizations, and biological applications. *Chem. Rev.* **2008**, *108*, 2064–2110. [CrossRef]
38. Teja, A.S.; Koh, P.-Y. Synthesis, properties, and applications of magnetic iron oxide nanoparticles. *Prog. Cryst. Growth Charact. Mater.* **2009**, *55*, 22–45. [CrossRef]
39. Heiba, Z.K.; Ahmed, S.I.; Mohamed, M.B. Effects of composition ratio of nano ZnS on structural and optical characteristics of Eu-doped maghemite/ZnS nanocomposite system. *Appl. Phys. A* **2022**, *128*, 633. [CrossRef]
40. Sherman, D.M. The electronic structures of Fe^{3+} coordination sites in iron oxides: Applications to spectra, bonding, and magnetism. *Phys. Chem. Miner.* **1985**, *12*, 161–175. [CrossRef]
41. Shokrollahi, H. A review of the magnetic properties, synthesis methods and applications of maghemite. *J. Magn. Magn. Mater.* **2017**, *426*, 74–81. [CrossRef]
42. Kosmulski, M. Compilation of PZC and IEP of sparingly soluble metal oxides and hydroxides from literature. *Adv. Colloid Interface Sci.* **2009**, *152*, 14–25. [CrossRef]
43. Jarlbring, M.; Gunneriusson, L.; Hussmann, B.; Forsling, W. Surface complex characteristics of synthetic maghemite and hematite in aqueous suspensions. *J. Colloid Interface Sci.* **2005**, *285*, 212–217. [CrossRef]
44. Das, S.; Hendry, M.J.; Essilfie-Dughan, J. Transformation of Two-Line Ferrihydrite to Goethite and Hematite as a Function of pH and Temperature. *Environ. Sci. Technol.* **2011**, *45*, 268–275. [CrossRef] [PubMed]
45. Hansel, C.M.; Benner, S.G.; Nico, P.; Fendorf, S. Structural constraints of ferric (hydr)oxides on dissimilatory iron reduction and the fate of Fe(II). *Geochim. Cosmochim. Acta* **2004**, *68*, 3217–3229. [CrossRef]
46. Sakurai, S.; Namai, A.; Hashimoto, K.; Ohkoshi, S.-I. First observation of phase transformation of all four Fe_2O_3 phases ($\gamma \rightarrow \varepsilon \rightarrow \beta \rightarrow \alpha$-phase). *J. Am. Chem. Soc.* **2009**, *131*, 18299–18303. [CrossRef] [PubMed]
47. Blake, R.; Hessevick, R.; Zoltai, T.; Finger, L.W. Refinement of the hematite structure. *Am. Mineral. J. Earth Planet. Mater.* **1966**, *51*, 123–129.
48. Schöttner, L.; Ovcharenko, R.; Nefedov, A.; Voloshina, E.; Wang, Y.; Sauer, J.; Wöll, C. Interaction of Water Molecules with the α-Fe_2O_3(0001) Surface: A Combined Experimental and Computational Study. *J. Phys. Chem. C* **2019**, *123*, 8324–8335. [CrossRef]
49. Souvi, S.M.O.; Badawi, M.; Paul, J.-F.; Cristol, S.; Cantrel, L. A DFT study of the hematite surface state in the presence of H_2, H_2O and O_2. *Surf. Sci.* **2013**, *610*, 7–15. [CrossRef]
50. Zhang, H.; Xu, Z.; Chen, D.; Hu, B.; Zhou, Q.; Chen, S.; Li, S.; Sun, W.; Zhang, C. Adsorption mechanism of water molecules on hematite (104) surface and the hydration microstructure. *Appl. Surf. Sci.* **2021**, *550*, 149328. [CrossRef]
51. Liu, J.; Zhu, R.; Ma, L.; Fu, H.; Lin, X.; Parker, S.C.; Molinari, M. Adsorption of phosphate and cadmium on iron (oxyhydr) oxides: A comparative study on ferrihydrite, goethite, and hematite. *Geoderma* **2021**, *383*, 114799. [CrossRef]
52. Cromières, L.; Moulin, V.; Fourest, B.; Giffaut, E. Physico-chemical characterization of the colloidal hematite/water interface: Experimentation and modelling. *Colloids Surf. A Physicochem. Eng. Asp.* **2002**, *202*, 101–115. [CrossRef]
53. Huang, Z.; Han, F.; Li, M.; Zhou, Z.; Guan, X.; Guo, L. Which phase of iron oxyhydroxides (FeOOH) is more competent in overall water splitting as a photocatalyst, goethite, akaganeite or lepidocrocite? A DFT-based investigation. *Comput. Mater. Sci.* **2019**, *169*, 109110. [CrossRef]
54. Zhao, J.-W.; Wang, H.-Y.; Feng, L.; Zhu, J.-Z.; Liu, J.-X.; Li, W.-X. Crystal-Phase Engineering in Heterogeneous Catalysis. *Chem. Rev.* **2024**, *124*, 164–209. [CrossRef] [PubMed]
55. Chakraborty, M.; Ghosh, A.; Thangavel, R.; Asokan, K. Conduction mechanism in mesoporous hematite thin films using low temperature electrical measurements and theoretical electronic band structure calculations. *J. Alloys Compd.* **2016**, *664*, 682–689. [CrossRef]
56. Liao, P.; Carter, E.A. Hole transport in pure and doped hematite. *J. Appl. Phys.* **2012**, *112*, 013701. [CrossRef]
57. Navrotsky, A.; Mazeina, L.; Majzlan, J. Size-driven structural and thermodynamic complexity in iron oxides. *Science* **2008**, *319*, 1635–1638. [CrossRef]
58. Namayandeh, A.; Borkiewicz, O.J.; Bompoti, N.M.; Chrysochoou, M.; Michel, F.M. Oxyanion surface complexes control the kinetics and pathway of ferrihydrite transformation to goethite and hematite. *Environ. Sci. Technol.* **2022**, *56*, 15672–15684. [CrossRef]
59. Barrón, V.; Torrent, J. Surface hydroxyl configuration of various crystal faces of hematite and goethite. *J. Colloid Interface Sci.* **1996**, *177*, 407–410. [CrossRef]
60. Hiemstra, T.; Van Riemsdijk, W.H. A surface structural approach to ion adsorption: The charge distribution (CD) model. *J. Colloid Interface Sci.* **1996**, *179*, 488–508. [CrossRef]
61. Wang, F.; Xu, J.; Xu, Y.; Chen, H.; Liang, Y.; Xiong, J. Face-dependent phosphate speciation on goethite: CD-MUSIC modeling and ATR-FTIR/2D-COS study. *Sci. Total Environ.* **2024**, *915*, 169970. [CrossRef]
62. Boily, J.-F. Water structure and hydrogen bonding at goethite/water interfaces: Implications for proton affinities. *J. Phys. Chem. C* **2012**, *116*, 4714–4724. [CrossRef]

63. Sherman, D.M. Electronic structures of iron (III) and manganese (IV)(hydr) oxide minerals: Thermodynamics of photochemical reductive dissolution in aquatic environments. *Geochim. Cosmochim. Acta* **2005**, *69*, 3249–3255. [CrossRef]
64. Shao, Y.; Hu, G.; Liu, Z.; Xu, X.; Zhang, M.; Ding, C.; Li, Y. Determination of band structure of naturally occurring goethite with Al substitution: A case study of Zhushan iron zone. *Materials* **2022**, *15*, 1465. [CrossRef] [PubMed]
65. Xu, P.; Zeng, G.M.; Huang, D.L.; Feng, C.L.; Hu, S.; Zhao, M.H.; Lai, C.; Wei, Z.; Huang, C.; Xie, G.X. Use of iron oxide nanomaterials in wastewater treatment: A review. *Sci. Total Environ.* **2012**, *424*, 1–10. [CrossRef] [PubMed]
66. Zhukhlistov, A. Crystal structure of lepidocrocite FeO (OH) from the electron-diffractometry data. *Crystallogr. Rep.* **2001**, *46*, 730–733. [CrossRef]
67. Guo, H.; Barnard, A.S. Proton transfer in the hydrogen-bonded chains of lepidocrocite: A computational study. *Phys. Chem. Chem. Phys.* **2011**, *13*, 17864–17869. [CrossRef]
68. Schwertmann, U.; Taylor, R. Natural and synthetic poorly crystallized lepidocrocite. *Clay Miner.* **1979**, *14*, 285–293. [CrossRef]
69. Majzlan, J.; Grevel, K.-D.; Navrotsky, A. Thermodynamics of Fe oxides: Part II. Enthalpies of formation and relative stability of goethite (α-FeOOH), lepidocrocite (γ-FeOOH), and maghemite (γ-Fe_2O_3). *Am. Mineral.* **2003**, *88*, 855–859. [CrossRef]
70. Schwertmann, U.; Taylor, R. The transformation of lepidocrocite to goethite. *Clays Clay Miner.* **1972**, *20*, 151–158. [CrossRef]
71. Hansel, C.M.; Benner, S.G.; Neiss, J.; Dohnalkova, A.; Kukkadapu, R.K.; Fendorf, S. Secondary mineralization pathways induced by dissimilatory iron reduction of ferrihydrite under advective flow. *Geochim. Cosmochim. Acta* **2003**, *67*, 2977–2992. [CrossRef]
72. Appelo, C.; Van der Weiden, M.; Tournassat, C.; Charlet, L. Surface complexation of ferrous iron and carbonate on ferrihydrite and the mobilization of arsenic. *Environ. Sci. Technol.* **2002**, *36*, 3096–3103. [CrossRef]
73. Kosmulski, M. The pH dependent surface charging and points of zero charge. VI. Update. *J. Colloid Interface Sci.* **2014**, *426*, 209–212. [CrossRef] [PubMed]
74. Stramel, R.; Thomas, J. Photochemistry of iron oxide colloids. *J. Colloid Interface Sci.* **1986**, *110*, 121–129. [CrossRef]
75. Michel, F.M.; Ehm, L.; Antao, S.M.; Lee, P.L.; Chupas, P.J.; Liu, G.; Strongin, D.R.; Schoonen, M.A.A.; Phillips, B.L.; Parise, J.B. The Structure of Ferrihydrite, a Nanocrystalline Material. *Science* **2007**, *316*, 1726–1729. [CrossRef] [PubMed]
76. Maillot, F.; Morin, G.; Juillot, F.; Bruneel, O.; Moulin, C.C.; Briois, V.; Calas, G.; Benedetti, M.F. New Insight into the Structure of Nanocrystalline Ferrihydrite: EXAFS Evidence for Tetrahedrally Coordinated Iron(III). *Geochim. Cosmochim. Acta* **2011**, *75*, 2708–2720. [CrossRef]
77. Sassi, M.; Chaka, A.M.; Rosso, K.M. Ab Initio Thermodynamics Reveals the Nanocomposite Structure of Ferrihydrite. *Commun. Chem.* **2021**, *4*, 134. [CrossRef]
78. Funnell, N.P.; Fulford, M.F.; Inoué, S.; Kletetschka, K.; Michel, F.M.; Goodwin, A.L. Nanocomposite Structure of Two-Line Ferrihydrite Powder from Total Scattering. *Commun. Chem.* **2020**, *3*, 22. [CrossRef]
79. Mendez, J.C.; Hiemstra, T. Surface Area of Ferrihydrite Consistently Related to Primary Surface Charge, Ion Pair Formation, and Specific Ion Adsorption. *Chem. Geol.* **2020**, *532*, 119304. [CrossRef]
80. Hiemstra, T.; Van Riemsdijk, W.H. A Surface Structural Model for Ferrihydrite I: Sites Related to Primary Charge, Molar Mass, and Mass Density. *Geochim. Cosmochim. Acta* **2009**, *73*, 4423–4436. [CrossRef]
81. Wang, P.; Li, D.; Chi, H.; Zhao, Y.; Wang, J.; Li, D.; Pang, S.; Fu, P.; Shi, J.; Li, C. Unveiling the Hydration Structure of Ferrihydrite for Hole Storage in Photoelectrochemical Water Oxidation. *Angew. Chem. Int. Ed.* **2021**, *60*, 6691–6698. [CrossRef]
82. Liu, J.; Sheng, A.; Li, X.; Arai, Y.; Ding, Y.; Nie, M.; Yan, M.; Rosso, K.M. Understanding the Importance of Labile Fe(III) during Fe(II)-Catalyzed Transformation of Metastable Iron Oxyhydroxides. *Environ. Sci. Technol.* **2022**, *56*, 3801–3811. [CrossRef]
83. Engel, M.; Noël, V.; Pierce, S.; Kovarik, L.; Kukkadapu, R.K.; Pacheco, J.S.L.; Qafoku, O.; Runyon, J.R.; Chorover, J.; Zhou, W.; et al. Structure and Composition of Natural Ferrihydrite Nano-Colloids in Anoxic Groundwater. *Water Res.* **2023**, *238*, 119990. [CrossRef] [PubMed]
84. Hu, J.; Li, S.; Chu, J.; Niu, S.; Wang, J.; Du, Y.; Li, Z.; Han, X.; Xu, P. Understanding the Phase-Induced Electrocatalytic Oxygen Evolution Reaction Activity on FeOOH Nanostructures. *ACS Catal.* **2019**, *9*, 10705–10711. [CrossRef]
85. Dai, Y.; Bostick, B.C.; Du, H.; Gu, X.; Huang, G.; Liu, S.; Song, L.; Liu, Y.; Ning, Z.; Sun, J.; et al. The Overlooked Role of Mineral Pore Geometry in the Solid-Solution Partitioning of (Poly)Oxyanionic Metals. *Geochim. Cosmochim. Acta* **2025**, *394*, 393–404. [CrossRef]
86. Lai, L.; He, Y.; Zhou, H.; Huang, B.; Yao, G.; Lai, B. Critical review of natural iron-based minerals used as heterogeneous catalysts in peroxide activation processes: Characteristics, applications and mechanisms. *J. Hazard. Mater.* **2021**, *416*, 125809. [CrossRef]
87. Vafaei Molamahmood, H.; Geng, W.; Wei, Y.; Miao, J.; Yu, S.; Shahi, A.; Chen, C.; Long, M. Catalyzed H_2O_2 Decomposition over Iron Oxides and Oxyhydroxides: Insights from Oxygen Production and Organic Degradation. *Chemosphere* **2022**, *291*, 133037. [CrossRef]
88. Huang, W.; Yuan, Y.; Zhong, D.; Zhang, P.; Liangdy, A.; Lim, T.-T.; Ma, W.; Yuan, Y. Catalytic activity of H_2O_2 by goethite and lepidocrocite: Insight from 5-bromosalicylic acid removal mechanism and density functional theory calculation. *Chemosphere* **2023**, *329*, 138551. [CrossRef]

89. Xu, H.; Wang, M.; Hei, S.; Qi, X.; Zhang, X.; Liang, P.; Fu, W.; Pan, B.; Huang, X. Neglected Role of Iron Redox Cycle in Direct Interspecies Electron Transfer in Anaerobic Methanogenesis: Inspired from Biogeochemical Processes. *Water Res.* **2024**, *262*, 122125. [CrossRef]
90. Qin, M.; Lu, B.; Feng, S.; Zhen, Z.; Chen, R.; Liu, H. Role of exposed facets and surface OH groups in the Fenton-like reactivity of lepidocrocite catalyst. *Chemosphere* **2019**, *230*, 286–293. [CrossRef]
91. Liu, Y.; Hu, P.; Wang, H. Computationally revisiting pH- and ligand-dependence of Fenton reaction selectivity and activity in aqueous solution. *Phys. Chem. Chem. Phys.* **2025**, *27*, 12929–12937. [CrossRef]
92. Kwan, W.P.; Voelker, B.M. Rates of hydroxyl radical generation and organic compound oxidation in mineral-catalyzed Fenton-like systems. *Environ. Sci. Technol.* **2003**, *37*, 1150–1158. [CrossRef]
93. Lin, S.S.; Gurol, M.D. Catalytic decomposition of hydrogen peroxide on iron oxide: Kinetics, mechanism, and implications. *Environ. Sci. Technol.* **1998**, *32*, 1417–1423. [CrossRef]
94. Wang, X.B.; Chen, N.; Liu, X.F.; Shi, Y.B.; Ling, C.C.; Zhang, L.Z. Ascorbate guided conversion of hydrogen peroxide to hydroxyl radical on goethite. *Appl. Catal. B Environ. Energy* **2021**, *282*, 119558. [CrossRef]
95. Munoz, M.; Conde, J.; de Pedro, Z.M.; Casas, J.A. Antibiotics abatement in synthetic and real aqueous matrices by H_2O_2/natural magnetite. *Catal. Today* **2018**, *313*, 142–147. [CrossRef]
96. Sun, F.W.; Liu, H.B.; Wang, H.L.; Shu, D.B.; Chen, T.H.; Zou, X.H.; Huang, F.J.; Chen, D. A novel discovery of a heterogeneous Fenton-like system based on natural siderite: A wide range of pH values from 3 to 9. *Sci. Total Environ.* **2020**, *698*, 134293. [CrossRef]
97. Chen, Y.F.; Miller, C.J.; Waite, T.D. Heterogeneous Fenton Chemistry Revisited: Mechanistic Insights from Ferrihydrite-Mediated Oxidation of Formate and Oxalate. *Environ. Sci. Technol.* **2021**, *55*, 14414–14425. [CrossRef]
98. Zhang, S.; Sun, M.; Hedtke, T.; Deshmukh, A.; Zhou, X.C.; Weon, S.; Elimelech, M.; Kim, J.H. Mechanism of Heterogeneous Fenton Reaction Kinetics Enhancement under Nanoscale Spatial Confinement. *Environ. Sci. Technol.* **2020**, *54*, 10868–10875. [CrossRef]
99. Hug, S.J.; Leupin, O. Iron-catalyzed oxidation of arsenic(III) by oxygen and by hydrogen peroxide: pH-dependent formation of oxidants in the Fenton reaction. *Environ. Sci. Technol.* **2003**, *37*, 2734–2742. [CrossRef]
100. Pestovsky, O.; Stoian, S.; Bominaar, E.L.; Shan, X.P.; Münck, E.; Que, L., Jr.; Bakac, A. Aqueous Fe=O: Spectroscopic identification and oxo-group exchange. *Angew. Chem. Int. Ed.* **2005**, *44*, 6871–6874. [CrossRef]
101. Bataineh, H.; Pestovsky, O.; Bakac, A. pH-induced mechanistic changeover from hydroxyl radicals to iron(IV) in the Fenton reaction. *Chem. Sci.* **2012**, *3*, 1594–1599. [CrossRef]
102. Chen, Y.F.; Miller, C.J.; Waite, T.D. pH Dependence of Hydroxyl Radical, Ferryl, and/or Ferric Peroxo Species Generation in the Heterogeneous Fenton Process. *Environ. Sci. Technol.* **2022**, *56*, 1278–1288. [CrossRef]
103. Chen, Y.; Miller, C.J.; Xie, J.; Waite, T.D. Challenges Relating to the Quantification of Ferryl(IV) Ion and Hydroxyl Radical Generation Rates Using Methyl Phenyl Sulfoxide (PMSO), Phthalhydrazide, and Benzoic Acid as Probe Compounds in the Homogeneous Fenton Reaction. *Environ. Sci. Technol.* **2023**, *57*, 18617–18625. [CrossRef]
104. Böhme, K.; Brauer, H. Generation of singlet oxygen from hydrogen peroxide disproportionation catalyzed by molybdate ions. *Inorg. Chem.* **1992**, *31*, 3468–3471. [CrossRef]
105. Yang, Z.; Qian, J.; Yu, A.; Pan, B. Singlet oxygen mediated iron-based Fenton-like catalysis under nanoconfinement. *Proc. Natl. Acad. Sci. USA* **2019**, *116*, 6659–6664. [CrossRef] [PubMed]
106. Moan, J.; Wold, E. Detection of singlet oxygen production by ESR. *Nature* **1979**, *279*, 450–451. [CrossRef] [PubMed]
107. Song, B.; Wang, G.; Tan, M.; Yuan, J. A europium (III) complex as an efficient singlet oxygen luminescence probe. *J. Am. Chem. Soc.* **2006**, *128*, 13442–13450. [CrossRef] [PubMed]
108. Miyamoto, S.; Martinez, G.R.; Medeiros, M.H.; Di Mascio, P. Singlet molecular oxygen generated from lipid hydroperoxides by the Russell mechanism: Studies using ^{18}O-labeled linoleic acid hydroperoxide and monomol light emission measurements. *J. Am. Chem. Soc.* **2003**, *125*, 6172–6179. [CrossRef]
109. Miyamoto, S.; Martinez, G.R.; Martins, A.P.B.; Medeiros, M.H.; Di Mascio, P. Direct evidence of singlet molecular oxygen [O_2 ($^1\Delta_g$)] production in the reaction of linoleic acid hydroperoxide with peroxynitrite. *J. Am. Chem. Soc.* **2003**, *125*, 4510–4517. [CrossRef]
110. Braun, A.M.; Dahn, H.; Gassmann, E.; Gerothanassis, I.; Jakob, L.; Kateva, J.; Martinez, C.G.; Oliveros, E. (2+4)-Cycloaddition with Singlet Oxygen. ^{17}O-lnvestigation of the Reactivity of Furfuryl Alcohol Endoperoxide. *Photochem. Photobiol.* **1999**, *70*, 868–874. [CrossRef]
111. Halladja, S.; Ter Halle, A.; Aguer, J.-P.; Boulkamh, A.; Richard, C. Inhibition of humic substances mediated photooxygenation of furfuryl alcohol by 2, 4, 6-trimethylphenol. Evidence for reactivity of the phenol with humic triplet excited states. *Environ. Sci. Technol.* **2007**, *41*, 6066–6073. [CrossRef]
112. Scaria, J.; Nidheesh, P.V. The role of non-radical pathway in heterogeneous activation of persulfate and H_2O_2 by superparamagnetic magnetite-reduced graphene oxide nanocomposite. *Sep. Purif. Technol.* **2022**, *299*, 121764. [CrossRef]

113. Nidheesh, P.V.; Boczkaj, G.; Ganiyu, S.O.; Oladipo, A.A.; Fedorov, K.; Xiao, R.Y.; Dionysiou, D.D. Generation, properties, and applications of singlet oxygen for wastewater treatment: A review. *Environ. Chem. Lett.* **2025**, *23*, 195–240. [CrossRef]
114. Xu, L.J.; Wang, J.L. Fenton-like degradation of 2,4-dichlorophenol using Fe_3O_4 magnetic nanoparticles. *Appl. Catal. B-Environ.* **2012**, *123*, 117–126. [CrossRef]
115. Shuai, W.J.; Gu, C.; Fang, G.D.; Zhou, D.M.; Gao, J. Effects of iron (hydr)oxides on the degradation of diethyl phthalate ester in heterogeneous (photo)-Fenton reactions. *J. Environ. Sci.* **2019**, *80*, 5–13. [CrossRef] [PubMed]
116. Chen, L.; Yang, Z.C.; Qian, J.S.; Pan, B.C. Interaction between Organic Compounds and Catalyst Steers the Oxidation Pathway and Mechanism in the Iron Oxide-Based Heterogeneous Fenton System. *Environ. Sci. Technol.* **2022**, *56*, 14059–14068. [CrossRef] [PubMed]
117. Zhang, R.; Chen, L.; Liang, Q.; Xi, J.; Zhao, H.; Jin, Y.; Gao, X.; Yan, X.; Gao, L.; Fan, K. Unveiling the Active Sites on Ferrihydrite with Apparent Catalase-like Activity for Potentiating Radiotherapy. *Nano Today* **2021**, *41*, 101317. [CrossRef]
118. Wang, X.; Wang, J.Q.; Cui, Z.T.; Wang, S.G.; Cao, M.H. Facet effect of α-Fe_2O_3 crystals on photocatalytic performance in the photo-Fenton reaction. *RSC Adv.* **2014**, *4*, 34387–34394. [CrossRef]
119. Huang, X.; Hou, X.; Zhao, J.; Zhang, L. Hematite facet confined ferrous ions as high efficient Fenton catalysts to degrade organic contaminants by lowering H_2O_2 decomposition energetic span. *Appl. Catal. B Environ.* **2016**, *181*, 127–137. [CrossRef]
120. Huang, X.; Chen, Y.; Walter, E.; Zong, M.; Wang, Y.; Zhang, X.; Qafoku, O.; Wang, Z.; Rosso, K.M. Facet-Specific Photocatalytic Degradation of Organics by Heterogeneous Fenton Chemistry on Hematite Nanoparticles. *Environ. Sci. Technol.* **2019**, *53*, 10197–10207. [CrossRef]
121. Choquehuanca, A.; Ruiz-Montoya, J.G.; Gómez, A.L.T. Discoloration of methylene blue at neutral pH by heterogeneous photo-Fenton-like reactions using crystalline and amorphous iron oxides. *Open Chem.* **2021**, *19*, 1009–1020. [CrossRef]
122. Wang, J.Y.; Wu, B.B.; Zheng, X.S.; Ma, J.Y.; Yu, W.C.; Chen, B.L.; Chu, C.H. Insights into the Crystallinity-Dependent Photochemical Productions of Reactive Oxygen Species from Iron Minerals. *Environ. Sci. Technol.* **2024**, *58*, 10623–10631. [CrossRef]
123. Zhong, Y.H.; Yu, L.; Chen, Z.F.; He, H.P.; Ye, F.; Cheng, G.; Zhang, Q.X. Microwave-Assisted Synthesis of Fe_3O_4 Nanocrystals with Predominantly Exposed Facets and Their Heterogeneous UVA/Fenton Catalytic Activity. *Acs Appl. Mater. Interfaces* **2017**, *9*, 29203–29212. [CrossRef] [PubMed]
124. Wu, Y.B.; Dai, C.; Nie, Y.L.; Tian, X.K.; Yang, C. Effect of morphology especially leaf-like morphology on surface Fe content of a-Fe_2O_3 in photo-assisted fenton-like degradation of organic contaminants. *Colloids Surf. A-Physicochem. Eng. Asp.* **2023**, *663*, 131116. [CrossRef]
125. Aeppli, M.; Voegelin, A.; Gorski, C.A.; Hofstetter, T.B.; Sander, M. Mediated Electrochemical Reduction of Iron (Oxyhydr-)Oxides under Defined Thermodynamic Boundary Conditions. *Environ. Sci. Technol.* **2018**, *52*, 560–570. [CrossRef] [PubMed]
126. Yu, C.L.; Ji, W.W.; Li, X.Y.; Yuan, S.H.; Zhang, P.; Pu, S.Y. Critical Role of Mineral Fe(IV) Formation in Low Hydroxyl Radical Yields during Fe(II)-Bearing Clay Mineral Oxygenation. *Environ. Sci. Technol.* **2024**, *58*, 9669–9678. [CrossRef]
127. Chen, P.; Song, D.; Liu, T.Y.; Chen, Y.; Zhou, Y.D.; Prange, M.P.; Chen, T.H.; Wang, D.Z.; Zhao, Y.T.; Wang, X.; et al. Facet-dependent Heterogeneous Fenton Reaction Mechanisms on Hematite Nanoparticles for (Photo)catalytic Degradation of Organic Dyes. *Adv. Sci.* **2025**, *12*, e08058. [CrossRef]
128. Al-Ahmari, F.; Al-Zahrani, A.; Al-Ghamdi, A. Comparative Study on the Adsorption Capacity of Goethite and Hematite towards Organic Contaminants: The Role of Surface Hydroxyl Density. *J. Environ. Chem. Eng.* **2021**, *9*, 105432.
129. Chen, S.X.; Liang, J.X.; Li, J.D.; Bao, C.Y.; Chen, Y.S.; Yue, D.T.; Fan, M.H.; Li, K.; Jia, J.P. Regulation of Surface Terminal Hydroxyl Coverage of FeOCl Catalyst via Crystal Facet Protection for Enhanced H_2O_2 Activation. *Environ. Sci. Technol.* **2025**, *59*, 10620–10630. [CrossRef]
130. Hou, X.; Huang, X.; Jia, F.; Ai, Z.; Zhao, J.; Zhang, L. Hydroxylamine Promoted Goethite Surface Fenton Degradation of Organic Pollutants. *Environ. Sci. Technol.* **2017**, *51*, 5118–5126. [CrossRef]
131. Huang, Q.Q.; Liu, H.Z.; Huang, M.J.; Wang, J.; Yu, H.Q. Ligand-assisted heterogeneous catalytic H_2O_2 activation for pollutant degradation: The trade-off between coordination site passivation and adjacent site activation. *Appl. Catal. B Environ. Energy* **2024**, *342*, 123403. [CrossRef]
132. Boland, D.D.; Collins, R.N.; Miller, C.J.; Glover, C.J.; Waite, T.D. Effect of Solution and Solid-Phase Conditions on the Fe(II)-Accelerated Transformation of Ferrihydrite to Lepidocrocite and Goethite. *Environ. Sci. Technol.* **2014**, *48*, 5477–5485. [CrossRef]
133. Pham, A.L.T.; Doyle, F.M.; Sedlak, D.L. Kinetics and efficiency of H_2O_2 activation by iron-containing minerals and aquifer materials. *Water Res.* **2012**, *46*, 6454–6462. [CrossRef] [PubMed]
134. Xie, H.; Li, Y.Z.; Jin, S.F.; Han, J.J.; Zhao, X.J. Facile Fabrication of 3D-Ordered Macroporous Nanocrystalline Iron Oxide Films with Highly Efficient Visible Light Induced Photocatalytic Activity. *J. Phys. Chem. C* **2010**, *114*, 9706–9712. [CrossRef]
135. Lu, J.-Y.; Yuan, Y.-R.; Hu, X.; Liu, W.-J.; Li, C.-X.; Liu, H.-Q.; Li, W.-W. MOF-Derived Fe_2O_3/Nitrogen/Carbon Composite as a Stable Heterogeneous Electro-Fenton Catalyst. *Ind. Eng. Chem. Res.* **2020**, *59*, 1800–1808. [CrossRef]

136. Tiya-Djowe, A.; Ruth, N.; Kamgang-Youbi, G.; Acayanka, E.; Laminsi, S.; Gaigneaux, E.M. FeO-kaolinite catalysts prepared via a plasma-assisted hydrolytic precipitation approach for Fenton-like reaction. *Microporous Mesoporous Mater.* **2018**, *255*, 148–155. [CrossRef]
137. Bondarenko, L.; Baimuratova, R.; Dzeranov, A.; Pankratov, D.; Kicheeva, A.; Sushko, E.; Kudryasheva, N.; Valeev, R.; Tropskaya, N.; Dzhardimalieva, G.; et al. Fenton reaction-driven pro-oxidant synergy of ascorbic acid and iron oxide nanoparticles in MIL-88B(Fe). *New J. Chem.* **2024**, *48*, 10142–10160. [CrossRef]
138. Jin, H.; Tian, X.; Nie, Y.; Zhou, Z.; Yang, C.; Li, Y.; Lu, L. Oxygen Vacancy Promoted Heterogeneous Fenton-like Degradation of Ofloxacin at pH 3.2–9.0 by Cu Substituted Magnetic Fe_3O_4@FeOOH Nanocomposite. *Environ. Sci. Technol.* **2017**, *51*, 12699–12706. [CrossRef]
139. Wu, X.C.; Liu, T.F.; Ni, W.X.; Yang, H.; Huang, H.; He, S.W.; Li, C.Y.; Ning, H.; Wu, W.T.; Zhao, Q.S.; et al. Engineering controllable oxygen vacancy defects in iron hydroxide oxide immobilized on reduced graphene oxide for boosting visible light-driven photo-Fenton-like oxidation. *J. Colloid Interface Sci.* **2022**, *623*, 9–20. [CrossRef]
140. Chen, X.; Fu, W.; Yang, Z.; Yang, Y.; Li, Y.; Huang, H.; Zhang, X.; Pan, B. Enhanced H_2O_2 utilization efficiency in Fenton-like system for degradation of emerging contaminants: Oxygen vacancy-mediated activation of O_2. *Water Res.* **2023**, *230*, 119562. [CrossRef]
141. Li, Y.; Wang, J.; Xiang, Z.; Yang, J.; Yin, J.; Guo, X.; Wang, W. Mn doping accelerates regeneration of Fe^{2+} in FeOOH and promotes efficient H_2O_2 activation for degradation of As(III). *Colloids Surf. A Physicochem. Eng. Asp.* **2022**, *655*, 130166. [CrossRef]
142. Li, B.; Gao, N.; Liao, Y.; Zhang, Y.; Mao, Y. Photo-Fenton ceramic composite membrane with Ag-doped FeOOH film for synergistically enhanced dye removal. *J. Water Process Eng.* **2024**, *64*, 105728. [CrossRef]
143. Xu, J.; Li, Y.; Yuan, B.; Shen, C.; Fu, M.; Cui, H.; Sun, W. Large scale preparation of Cu-doped α-FeOOH nanoflowers and their photo-Fenton-like catalytic degradation of diclofenac sodium. *Chem. Eng. J.* **2016**, *291*, 174–183. [CrossRef]
144. Nguyen, X.S.; Zhang, G.; Yang, X. Mesocrystalline Zn-Doped Fe_3O_4 Hollow Submicrospheres: Formation Mechanism and Enhanced Photo-Fenton Catalytic Performance. *ACS Appl. Mater. Interf.* **2017**, *9*, 8900–8909. [CrossRef]
145. Sun, F.; Lu, T.; Feng, J.; Kang, Y. Dual-functional heterogeneous Fenton catalyst Cu/Ti co-doped Fe_3O_4@FeOOH for cyanide-containing wastewater treatment: Preparation, performance and mechanism. *Environ. Pollut.* **2024**, *345*, 123523. [CrossRef]
146. Tian, X.; Luo, T.; Nie, Y.; Shi, J.; Tian, Y.; Dionysiou, D.D.; Wang, Y. New Insight into a Fenton-like Reaction Mechanism over Sulfidated β-FeOOH: Key Role of Sulfidation in Efficient Iron(III) Reduction and Sulfate Radical Generation. *Environ. Sci. Technol.* **2022**, *56*, 5542–5551. [CrossRef]
147. Qian, X.; Ren, M.; Zhu, Y.; Yue, D.; Han, Y.; Jia, J.; Zhao, Y. Visible Light Assisted Heterogeneous Fenton-Like Degradation of Organic Pollutant via α-FeOOH/Mesoporous Carbon Composites. *Environ. Sci. Technol.* **2017**, *51*, 3993–4000. [CrossRef]
148. Su, S.S.; Liu, Y.Y.; Liu, X.M.; Jin, W.; Zhao, Y.P. Transformation pathway and degradation mechanism of methylene blue through β-FeOOH@GO catalyzed photo-Fenton-like system. *Chemosphere* **2019**, *218*, 83–92. [CrossRef] [PubMed]
149. Wang, X.; Liu, W.; Qin, J.; Lei, L. Improvement of H_2O_2 Utilization by the Persistent Heterogeneous Fenton Reaction with the Fe_3O_4-Zeolite-Cyclodextrin Composite. *Ind. Eng. Chem. Res.* **2020**, *59*, 2192–2202. [CrossRef]
150. Liu, R.; Li, R.; Yang, L.; Wang, R.-X.; Chen, H.-Y.; Wang, N.; Li, Z.; Chen, Y.-Q.; Ramakrishna, S.; Long, Y.-Z. FeOOH Quantum Dot-Coupled Z-Scheme $BiVO_4$/g-C_3N_4 Heterojunction for Enhancing Photo-Fenton Reactions. *ACS Appl. Nano Mater.* **2023**, *6*, 17009–17020. [CrossRef]

Disclaimer/Publisher's Note: The statements, opinions and data contained in all publications are solely those of the individual author(s) and contributor(s) and not of MDPI and/or the editor(s). MDPI and/or the editor(s) disclaim responsibility for any injury to people or property resulting from any ideas, methods, instructions or products referred to in the content.